J. Fluid Mech. (2006), *vol.* 567, *pp.* 27–63.
doi:10.1017/S0022112006001959 Printed in the United Kingdom

Experimental characterization of initial conditions and spatio-temporal evolution of a small-Atwood-number Rayleigh–Taylor mixing layer

By NICHOLAS J. MUESCHKE[1], MALCOLM J. ANDREWS[1]† AND OLEG SCHILLING[2]

[1]Department of Mechanical Engineering, Texas A&M University, College Station, TX 77843, USA
[2]University of California, Lawrence Livermore National Laboratory, Livermore, CA 94550, USA

(Received 17 October 2005 and in revised form 11 April 2006)

The initial multi-mode interfacial velocity and density perturbations present at the onset of a small-Atwood-number, incompressible, miscible Rayleigh–Taylor instability-driven mixing layer have been quantified using a combination of experimental techniques. The streamwise interfacial and spanwise interfacial perturbations were measured using high-resolution thermocouples and planar laser-induced fluorescence (PLIF), respectively. The initial multi-mode streamwise velocity perturbations at the two-fluid density interface were measured using particle-image velocimetry (PIV). It was found that the measured initial conditions describe an initially anisotropic state, in which the perturbations in the streamwise and spanwise directions are independent of one another. The evolution of various fluctuating velocity and density statistics, together with velocity and density variance spectra, were measured using PIV and high-resolution thermocouple data. The evolution of the velocity and density statistics is used to investigate the early-time evolution and the onset of strongly nonlinear, transitional dynamics within the mixing layer. The early-time evolution of the density and vertical velocity variance spectra indicate that velocity fluctuations are the dominant mechanism driving the instability development. The implications of the present experimental measurements on the initialization of Reynolds-averaged turbulent transport and mixing models and of direct and large-eddy simulations of Rayleigh–Taylor instability-induced turbulence are discussed.

1. Introduction

A complete understanding of the transitional dynamics in instability-driven turbulent flows remains a fundamental challenge for turbulence theory and modelling. Canonical two-fluid hydrodynamic instabilities, such as the Kelvin–Helmholtz (Helmholtz 1868; Kelvin 1871), Rayleigh–Taylor (Rayleigh 1884; Taylor 1950) and Richtmyer–Meshkov (Richtmyer 1960; Meshkov 1969) instabilities, develop from a quiescent or laminar state, become transitional, and eventually fully developed. Whereas the linear and weakly nonlinear theories for the growth of these shear- and buoyancy-driven instabilities are well developed (Chandrasekhar 1961; Brouillette

† Author to whom correspondence should be addressed.

2002; Drazin & Reid 2004), the transitional dynamics of such instability-driven flows and their fully turbulent state are not nearly as well understood. Transitional flows are difficult to treat analytically as they possess many of the chaotic properties of fully developed turbulent flows (Drazin 2002; Criminale, Jackson & Joslin 2003) including spatio-temporal evolution, inhomogeneity and anisotropy, intermittency of the transitional and free-stream flow and, in the case of interfacial hydrodynamic instabilities in which two or more fluids are present, species transport and molecular mixing. Further complications arise owing to the relatively poorly understood dependence of the transitional and turbulent flow generated by interfacial instabilities on the initial conditions (Husain & Hussain 1979; Dalziel, Linden & Youngs 1999; Cook & Dimotakis 2001; Mi, Nobes & Nathan 2001; Faisst & Eckhardt 2004; Ramaprabhu, Dimonte & Andrews 2005). An objective of the present work is to examine the evolution of a transitional flow induced by the Rayleigh–Taylor instability in detail as it approaches a fully developed turbulent state using state-of-the-art experimental diagnostics.

The transitional stage between the early-time growth of perturbations and fully developed turbulence has been studied experimentally in a variety of fluid configurations. Studies of transitional flows date back to the examination of the onset of turbulence in pipe flows (Reynolds 1883). More recently, Darbyshire & Mullin (1995) used sophisticated diagnostics and controlled perturbations in an experimental study of the transitional regime in pipe flows. Measurements of the initial conditions and the characterization of the transition to turbulence in planar shear layers have received considerable attention (Bradshaw 1966; Brown & Roshko 1974; Bell & Mehta 1993; Weygandt & Mehta 1995). Marmottant & Villermaux (2004) examined the initial perturbations of a liquid to investigate the growth of Kelvin–Helmholtz and Rayleigh–Taylor instabilities as the liquid jet transitioned to an atomized spray. Measurements of the initial conditions and of the transition stages in shear-layer flows have been well studied; however, the experimental characterization of the initial conditions and transition regime in buoyancy-driven turbulent mixing layers remains limited. Measurements of the initial multi-mode perturbations of interfacial instabilities have proved to be non-trivial, as evidenced by the paucity of experimental results in this area. The magnitudes of the interfacial position and velocity fluctuations are typically very small, and thus difficult to resolve experimentally in non-stationary flows. Dalziel *et al.* (1999) measured the velocity field generated by the removal of a thin barrier initially separating two fluids of different densities, which then interpenetrated and evolved into a turbulent mixing layer. Milovich *et al.* (2004) and Dimonte (2004) have reported measurements of initial perturbations on the exterior shell of an inertial confinement fusion (ICF) target. The goal of the present work is to completely and accurately quantify the perturbations present at the onset of a buoyancy-driven Rayleigh–Taylor mixing layer and to examine the development of the characteristics of a transitional mixing layer.

In addition, the complex dynamics that arise as a flow begins to develop characteristics of fully developed turbulence present several issues for the development of turbulent transport and mixing (Reynolds-averaged Navier–Stokes, RANS) models in the transitional regime. Modelling complex, multi-scale, variable-density turbulent flows characterized by an expanding range of time scales and length scales continues to represent a grand challenge for the turbulence community. The validation of predictive turbulent transport models of anisotropic, inhomogeneous, variable-density turbulence and mixing requires *a priori* knowledge of second- and higher-order correlations of velocity and density fluctuations, such as $\overline{\rho'^2}$, $\overline{u_i'u_j'}$, $\overline{\rho'u_j'}$ and

$\overline{u_i' u'^2/2 + p' u_i'}$, where the overbar denotes Reynolds averaging. Turbulent mixing layers induced by the Rayleigh–Taylor instability represent a special case in which the flow is initially quiescent or laminar, becomes transitional, and finally turbulent. Currently, the proper initialization of quantities required in turbulent transport models, such as the turbulent kinetic energy and its dissipation rate, or the coupling of the initial conditions to subgrid-scale models for large-eddy simulations (LES), is an open research topic in Rayleigh–Taylor instability-driven mixing. Thus, this work is partly motivated by the need for detailed experimental data to assess and to develop further both RANS and subgrid-scale models that include the effects of initial conditions on Rayleigh–Taylor instability-induced mixing.

To accomplish the principal objective of this investigation, the initial interfacial and velocity perturbations at the two-fluid interface of a small-Atwood-number Rayleigh–Taylor mixing layer were experimentally measured in a water channel facility at Texas A&M University. Also, the measured time-evolution of various velocity, density, mixing statistics and spectra is presented to further elucidate the role of initial conditions in the early-time development of a Rayleigh–Taylor instability-driven mixing layer. Details on the experimental facility are provided in § 3 and the experimental results are reported in § 4. Hence, this work provides detailed experimental measurements of the initial conditions and the early-time development of a buoyancy-driven mixing layer.

2. Previous experimental investigations of Rayleigh–Taylor instability and mixing

The Rayleigh–Taylor instability occurs when a heavy fluid with density ρ_1 is accelerated towards a lighter fluid with density ρ_2 and the fluid layers are initially separated by a perturbed interface (Rayleigh 1884; Taylor 1950). For the case considered here, the acceleration is that of Earth's gravity $g = 981\ \mathrm{cm\ s^{-2}}$. A Rayleigh–Taylor unstable stratification exists when the density and pressure gradients are oriented such that $\nabla\rho \cdot \nabla p < 0$. With small-amplitude perturbations at the two-fluid interface, each mode grows exponentially and independently at early times according to linear theory (Chandrasekhar 1961; Drazin & Reid 2004) until nonlinear modal interactions ensue (Sharp 1984; Haan 1989) and smaller modes merge to create larger buoyant structures: bubbles of lighter fluid 'rise' in the direction opposite to the acceleration, while spikes of heavier fluid 'fall' in the direction of the acceleration. Secondary Kelvin–Helmholtz instabilities grow as localized high-shear regions develop between the rising bubbles and the falling spikes (Sharp 1984). As the amplitude of a particular mode approaches approximately half its wavelength, the growth rate of that mode saturates (Youngs 1984). Finally, as the mixing layer becomes turbulent and grows in spatial extent, dimensional analysis shows that (in the absence of dissipative, diffusive, surface tension and other effects) the only relevant dynamical length scale is gt^2. In this late-time self-similar regime, the appropriately defined penetration of the bubble front in a mixing layer scales quadratically in time as

$$h_b(t) = \alpha A g t^2, \tag{1}$$

where $A \equiv (\rho_1 - \rho_2)/(\rho_1 + \rho_2) > 0$ is the Atwood number and α is a dimensionless function of the Atwood number, Reynolds number, and possibly other non-dimensional parameters (Anuchina *et al.* 1978; Youngs 1984; Cook & Dimotakis 2001). In the limit of very small Atwood number, as considered in the present work, h_b is approximately equal to the penetration of the spike front h_s. The determination

of the exact conditions under which the self-similarity implied by (1) is satisfied is currently an active area of investigation (Cook & Dimotakis 2001; Dimonte *et al.* 2004, 2005; Ramaprabhu & Andrews 2004*b*; Ristorcelli & Clark 2004; Cook, Cabot & Miller 2004) and is not further considered in the present work.

The focus of experiments and the sophistication of diagnostics employed in Rayleigh–Taylor mixing experiments have evolved considerably over the past fifty years, as briefly reviewed below. Initial studies examined two-dimensional single-mode Rayleigh–Taylor instabilities using ordinary photographic techniques, whereas more recent work has focused on the examination of the internal turbulent structure and initial conditions of multi-mode Rayleigh–Taylor mixing layers using sophisticated flow diagnostics. Early experiments by Allred, Blount & Miller (1954) used optical techniques to examine the development of Rayleigh–Taylor perturbations on a rising bubble front. Emmons, Chang & Watson (1960) pioneered the method of accelerating a tank containing two fluids of different densities, thereby creating a Rayleigh–Taylor unstable interface. They obtained an approximate single-mode perturbation at the density interface by oscillating a paddle, and measured the growth of individual bubbles and spikes using high-speed photography. Other workers have also used some type of accelerated tank containing miscible or immiscible fluids with different densities to investigate the growth of Rayleigh–Taylor instability-driven mixing layers (Cole & Tankin 1973; Ratafia 1973; Popil & Curzon 1979; Read 1984; Jacobs & Catton 1988; Kucherenko *et al.* 1994, 1997, 2003*a*, *b*; Dimonte & Schneider 1996, Dimonte 1999; Wilkinson 2004). Some experiments imposed an approximate sinusoidal perturbation at the two-fluid interface and primarily used ordinary photographic techniques to measure the growth of individual bubbles and spikes (Cole & Tankin 1973; Ratafia 1973; Popil & Curzon 1979; Jacobs & Catton 1988; Wilkinson 2004). In addition to the measurement of the mixing-layer width, Wilkinson (2004) used planar laser-induced fluorescence (PLIF) to measure the growth and internal structure of the single-mode three-dimensional Rayleigh–Taylor instability. Others have seeded multi-mode perturbations by either intentionally imposing broadbanded perturbations or allowing ambient noise to provide the necessary perturbations (Read 1984; Dimonte & Schneider 1996; Dimonte 1999; Kucherenko *et al.* 1997, 2003*a*, *b*). In this multi-mode case, optical techniques were used to measure the growth of the turbulent mixing layer, rather than the amplitudes of individual bubbles and spikes. Standard photographic techniques limited investigations to the quantification of the spatial growth of the mixing layer; measurements of the internal structure of the mixing layer, and the quantification of the degree of molecular mixing were not possible. An alternative to using standard photography is to measure mixing-layer widths using X-ray radiography (Kucherenko *et al.* 1997, 2003*a*). Kucherenko *et al.* (2003*a*) measured the growth of a miscible, turbulent Rayleigh–Taylor mixing layer for different sets of initial diffusion-layer thicknesses and small-scale random perturbations. Also, Kucherenko *et al.* (2003*b*) used laser-induced fluorescence (LIF) to measure the distribution of fluid fragment sizes within an immiscible, turbulent Rayleigh–Taylor mixing layer.

To avoid difficulties associated with the imaging of a flow in an accelerating tank, various workers have designed Rayleigh–Taylor experiments that were stationary in space. In one such experiment, a tank containing two fluids of different densities was rapidly overturned (Andrews 1986; Andrews & Spalding 1990). These experiments included adverse stratifications of fluids with nominally flat and tilted interfaces. The initial tilt angle of the two-fluid interface and growth of the mixing layer could be accurately measured using optical techniques, but the initial small-scale perturbations

could not be measured. In addition, no detailed data on the internal structure of the mixing layer were obtained. Another approach produced an unstable interface by withdrawing a plate that separated a heavier fluid situated above a lighter fluid in a tank (Linden & Redondo 1991; Linden, Redondo & Youngs 1994; Dalziel *et al.* 1999). These experiments also used optical techniques to measure the growth of the mixing layer and the average volume fraction profiles across the mixing layer. Densitometry was used to measure the degree of molecular mixing as a function of time. In addition, Dalziel *et al.* (1999) used a particle-tracking method to measure the velocity perturbations in a vertical plane introduced by the horizontal withdrawal of the splitter plate. The present work differs from Dalziel *et al.* (1999) in that they present the initial conditions of a transient Rayleigh–Taylor experiment, whereas this work characterizes the initial conditions of a statistically stationary Rayleigh–Taylor mixing layer.

Another method for generating a Rayleigh–Taylor unstable interface was pioneered by Snider & Andrews (1994), in which cold and hot water streams are initially separated by a thin splitter plate. After termination at the knife edge of the splitter plate, the resulting flow configuration is Rayleigh–Taylor unstable and a mixing layer develops downstream. The water channel of Snider & Andrews (1994) was used in the current investigation, and is discussed in detail in § 3. Optical techniques were used to measure the self-similar quadratic-in-time growth of the mixing layer and the average volume fraction (non-dimensional density) profiles across the mixing layer. High-resolution thermocouples and particle-image velocimetry (PIV) were used to investigate the velocity and density fluctuations within the mixing layer, the average volume fraction profiles across the layer, and the degree of molecular mixing within the layer (Wilson 2002; Wilson & Andrews 2002; Ramaprabhu 2003; Ramaprabhu & Andrews 2004*a*). Density and velocity variance (energy) spectra were also reported. PIV was also used to measure the components of the Reynolds stress tensor $\langle u'^2 \rangle$, $\langle w'^2 \rangle$ and $\langle u'w' \rangle$ at various downstream locations (Wilson 2002; Ramaprabhu 2003; Ramaprabhu & Andrews 2004*a*), where u and w are the streamwise and vertical velocity components, respectively, $u' = u - \langle u \rangle$ and $w' = w - \langle w \rangle$ are the corresponding fluctuating components, and the angle brackets denote a spatial average (see equation (5)). The same water-channel configuration was used to measure both large- and small-scale statistics (Ramaprabhu 2003; Ramaprabhu & Andrews 2004*a*), such as the components of the Reynolds stress anisotropy tensor $b_{ij} \equiv \langle u'_i u'_j \rangle / \langle u'^2 \rangle - \delta_{ij}/3$ (Pope 2000), where δ_{ij} is the Kronecker tensor. The PIV-S (scalar) technique was used to simultaneously measure two-dimensional density and velocity fields, yielding measurements of the density–velocity correlations $\langle \rho' u' \rangle$ and $\langle \rho' w' \rangle$ (Ramaprabhu & Andrews 2003) and the balance between potential energy, kinetic energy and dissipation. In addition to quantifying turbulence statistics, the initial density and velocity fluctuations were measured at the two-fluid interface in the streamwise direction (Ramaprabhu & Andrews 2004*a*, *b*). The current investigation provides additional quantitative data on the initial development of a Rayleigh–Taylor mixing layer using a combination of diagnostics, including thermocouples, particle-image velocimetry and planar laser-induced fluorescence, and will be discussed in § 4.

3. Experimental configuration

The water channel is an open-loop facility in which cold water and warm water (at a temperature difference $\Delta T \approx 5\,^{\circ}\mathrm{C}$), initially separated by a 3.2 mm thick Plexiglas

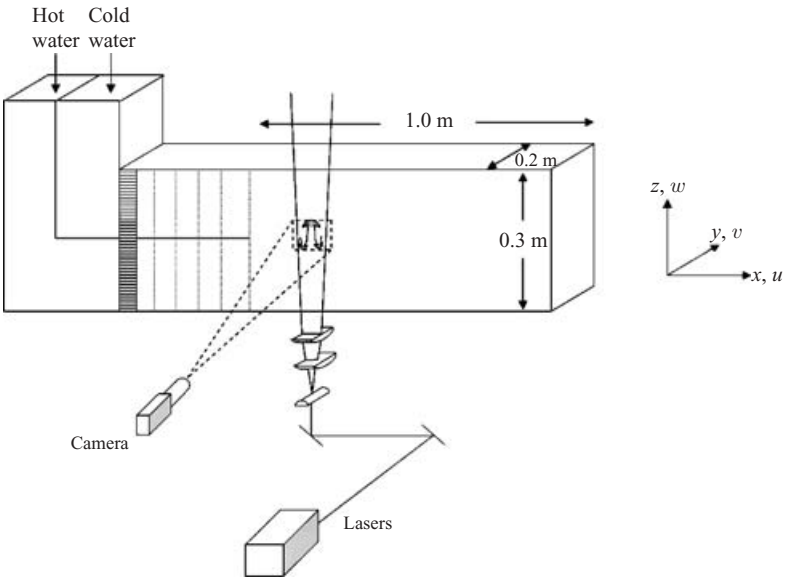

FIGURE 1. Schematic of the water channel and the associated diagnostics. The conventions for the coordinates and velocities are shown on the right-hand side. Camera: 640H $\times$ 480V pixels, 1200 image capacity on board, Thermocouple: E-type, 0.16 mm diameter, 100 kHz, sampling at 12 bit accuracy. Lasers: two 120 mJ Nd-YAG, 15 Hz pulse, sample rate 30 s^{-1}.

splitter plate, enter the channel horizontally. A schematic of the water channel, diagnostics and reference axes are shown in figure 1. A density difference between the two streams is induced by thermal expansion of the warmer water. The water channel is supplied from two 500 gallon water tanks; a typical experiment has a running time of approximately 10 min. Sump pumps in each tank ensure adequate stirring of the water to maintain temperature uniformity. Cold and hot water are pumped into the entrance plenum and each stream flows through an arrangement of flow-straighteners, followed by a series of screen meshes (30×30 wires/in). The screen meshes reduce the free-stream velocity fluctuations, and reduce the momentum deficit caused by boundary layers along the walls of the channel and splitter plate. The splitter plate terminates at a 2.5° knife-edge followed immediately by another screen mesh (35×35 wires/in). This final screen mesh (end-screen) minimizes the momentum deficit at the end of the splitter plate, thereby reducing the magnitude and wavelength of the wake shed from the splitter plate (Koop 1976; Browand & Weidman 1976; Stillinger *et al.* 1983).

Upon entering the mixing section of the channel, an adverse density stratification exists between the two water streams and a Rayleigh–Taylor instability-driven mixing layer forms downstream. The mixing section is 100 cm long (x-direction) with cross-sectional dimensions of 20 cm $\times$ 32 cm (width $\times$ height). In the present experiments, the mean advection velocity is $U_m \approx 4.75\,\mathrm{cm\,s^{-1}}$, with the two stream velocities matched so that there is no shear due to mean velocity gradients. The sidewalls have been shown to have negligible influence on the growth rate of the mixing layer (Snider & Andrews 1994). Water channel measurements have also been shown to be statistically stationary for higher-order moments of velocity and density fluctuations (Wilson 2002; Ramaprabhu 2003).

FIGURE 2. Photographic image of a water channel experiment. The mean flow is from left to right.

Parameter	Value	Description
ρ_1	$0.9986\,\mathrm{g\,cm^{-3}}$	Density of top (cold) stream
ρ_2	$0.9970\,\mathrm{g\,cm^{-3}}$	Density of bottom (warm) stream
A	7.5×10^{-4}	Atwood number
U_m	$4.75\,\mathrm{cm\,s^{-1}}$	Mean velocity
μ_1	$0.009\,\mathrm{g\,cm^{-1}\,s^{-1}}$	Dynamic viscosity of top stream
μ_2	$0.011\,\mathrm{g\,cm^{-1}\,s^{-1}}$	Dynamic viscosity of bottom stream
Pr	7.0	Prandtl number $Pr \equiv \nu/D$
H	32.0 cm	Total height of channel

TABLE 1. Parameters in a typical experiment.

To illustrate the spatial and temporal mixing-layer development within the water channel, an image of the mixing layer is shown in figure 2. Six grams of Nigrosene dye was added to the top stream for visualization purposes. Small interfacial perturbations, which are sub-pixel in size in figure 2, grow and interact to form the mixing layer seen on the right-hand side of the image. The downstream distance from the trailing edge of the splitter plate x is converted to time $t = x/U_m$ using Taylor's hypothesis (Taylor 1938; Pope 2000). Time is normalized by the characteristic buoyancy time scale (Snider & Andrews 1994; Dalziel *et al.* 1999; Ramaprabhu & Andrews 2004*a*)

$$\tau \equiv t\sqrt{\frac{Ag}{H}} = \frac{x}{U_m}\sqrt{\frac{Ag}{H}}, \tag{2}$$

where $H = 32\,\mathrm{cm}$ is the total height of the mixing-layer channel. The experimental parameters are summarized in table 1.

The primary objective of the current investigation is to measure the initial velocity and interfacial perturbations, and to determine their influence on the development of the mixing layer. To accomplish this, three separate and independent measurements were performed to quantify the initial conditions of the flow. Two different techniques were required to measure the initial density and interfacial perturbation in the streamwise (x) and spanwise (y) direction. A third technique was required to measure the initial velocity fluctuations. First, the *fluctuating density field* shed from the trailing-edge of the splitter plate was inferred from temperatures measured using a high-resolution thermocouple. Second, *velocity perturbations in the streamwise direction* were measured using particle-image velocimetry (PIV). Third, *interfacial perturbations in the spanwise direction* were measured using planar laser-induced

Downstream location x (cm)	Non-dimensional time τ
0.5	0.016
2.0	0.061
5.0	0.166
6.0	0.204
8.0	0.255
10.0	0.342
11.3	0.334
12.5	0.400
15.0	0.473
16.0	0.552
20.1	0.694
25.0	0.865
27.0	0.924
40.0	1.363

TABLE 2. Downstream locations of centreplane temperature (density) measurements and the corresponding non-dimensional times.

fluorescence (PLIF). In addition to quantifying the initial conditions, the evolution of the fluctuating velocity and density, as well as mixing statistics have been measured to study the transition from weakly to strongly nonlinear mixing. Details of each experimental method and of the corresponding measurements are presented in the next section.

4. Experimental measurements

4.1. *Thermocouple diagnostics and measurements of the streamwise interfacial perturbation*

4.1.1. *Thermocouple measurements and data acquisition system*

The measurement of the density perturbation in the streamwise (x) direction was performed using a high-resolution thermocouple temperature measurement system. Temperature fluctuations were measured using E-type thermocouples positioned at multiple downstream locations from the splitter plate (table 2). The thermocouples were constructed from 40 gauge wire (0.08 mm diameter) with a weld bead diameter of 0.16 mm – a smaller diameter than used previously in this water channel (Snider & Andrews 1994; Ramaprabhu & Andrews 2004*a*), resulting in a less intrusive diagnostic and improved spatial resolution. The time constant of the thermocouple was determined (Mills 1999) to be $t_c = 0.0047$ s with a corresponding frequency response of $1/(3t_c)$ i.e. 71 Hz (corresponding to $kH = 1500$, where $k = 2\pi/\lambda$). Mueschke & Andrews (2006) showed that these spatial resolution enhancements reduced the uncertainty in the mixing statistics and scalar fluctuation spectra. The thermocouple wire, extension wire, and all connections were shielded and grounded to minimize external electromagnetic and radio frequency noise. Temperature measurements were recorded at a rate of 50 kHz using a 16-bit data acquisition system. Spurious noise from the temperature trace was eliminated using a 50-point averaging window, thus reducing the sampling rate to 1 kHz. Hence, the window averaging procedure does not affect the temperature fluctuations measured by the thermocouple. Using Taylor's hypothesis, at a sampling rate of 1 kHz and a mean advection velocity of $U_m \approx 4.75\,\mathrm{cm\,s^{-1}}$, each pointwise temperature measurement was separated by 0.048 mm, which is

approximately 30 % of the diameter of the probe volume. Fluctuations of the temperature measurements at the Nyquist frequency (500 Hz) were below the system noise, obviating the need for a more complex filtering algorithm that retains spectral resolution. Temperatures were converted to density values using the equation of state of water

$$\rho(T) = \frac{999.8396 + 18.2249\,T - 0.007922\,T^2 - 55.448\times10^{-6}\,T^3 + 149.756\times10^{-9}\,T^4 - 393.295\times10^{-12}\,T^5}{1 + 18.159\times10^{-3}\,T} \tag{3}$$

in units of $\mathrm{kg\,m^{-3}}$ (Kukulka 1981). Hereinafter, density and temperature are used interchangeably, as they are related by (3).

Three measurements were performed to ensure an accurate measurement of the non-dimensional time τ, as x, U_m and A are parameters that can vary from one experiment to another and must be measured accurately to determine τ. First, the distance between the splitter plate and the probe volume was measured. Second, the Atwood number was measured using a digital temperature probe with a K-type thermocouple to measure the water temperature in each 500 gallon tank. Finally, the mean flow velocity in the water channel was measured as follows. The mean advection velocity of both streams was adjusted until no shear was present and $U_m \approx 4.5$–$5.0\,\mathrm{cm\,s^{-1}}$. The presence of a mean velocity gradient between the two streams was determined in several ways. The pumping system was regularly calibrated by injecting dye into the top and bottom streams and adjusting the flow rates to eliminate relative motion. In addition, dye was also injected onto the splitter plate just before the end-screen. Once the dye was entrained into the mixing layer, the 'lean' of developing Rayleigh–Taylor bubbles with respect to the vertical (z) axis was examined at downstream locations. In the absence of any 'leaning', the difference between the top and bottom stream velocities was shown to be at most $|U_1 - U_2| < 0.2\,\mathrm{cm\,s^{-1}}$ or $\sim$5% of the mean advection velocity (Ramaprabhu 2003). A final determination of the existence of shear was performed by examining the skew of the PDF of density (volume fraction) fluctuations. In the small-Atwood-number limit of the Rayleigh–Taylor instability, bubbles and spikes grow symmetrically. The symmetry in the geometry of the apparatus suggests that the PDF of the density fluctuations should also be symmetric, such that there is no skew in the PDF. Any measurement containing a skewed PDF due to the existence of excessive shear was discarded. To measure U_m, a syringe was used to inject fluid containing a high concentration of Nigrosene dye. The time t_m required for a blob of dye to travel a distance L_m from the end-screen to a marked downstream location was recorded, so that $U_m = L_m/t_m$.

4.1.2. *Determination of the density*

To measure the density values, a thermocouple was mounted on a thin vertical rod that allowed fine adjustment of the probe location in the vertical (z) direction. All measurements in the present study were performed at the centreplane of the mixing layer ($z = 0$), defined as the plane at which equal average volume fractions of hot and cold water exist, i.e. the centreplane corresponds to the position at which the average volume fraction of fluid 1

$$f_1 \equiv \frac{\rho(x) - \rho_2}{\rho_1 - \rho_2} \tag{4}$$

is $\langle f_1 \rangle = 1/2$, where the spatial (Reynolds) average of a scalar quantity $\phi(x, \tau)$ is defined as

$$\langle \phi \rangle(\tau) = \frac{1}{L} \int_0^L \phi(x, \tau)\, \mathrm{d}x. \tag{5}$$

Spatial averaging of pointwise measurements uses Taylor's hypothesis such that $x = U_m t$, $L \equiv U_m N_{samp}/f_{samp}$ is the distance (cm) over which $\phi(x, \tau)$ was measured, N_{samp} is the number of samples, and f_{samp} is the sampling rate (Hz).

The initial interface between the two fluids, and subsequent centreplane of the mixing layer that forms, is nominally a horizontal plane normal to the direction of gravity. However, as the splitter plate is not perfectly horizontal, the location of the centreplane drifts slightly. While the location of the centreplane of the mixing layer changes slightly with downstream distance, there is no evidence that the results presented are affected by this drift. In addition, it was concluded that a visual inspection of the thermocouple probe placement could not provide an accurate measure of the mixing-layer centreline with respect to (5). Consequently, the following procedure was used to position the probe accurately: a set of temperature measurements was recorded at 200 Hz and $\langle f_1 \rangle$ was evaluated; depending upon the value of $\langle f_1 \rangle$, the position of the probe was adjusted vertically until $\langle f_1 \rangle = 0.50 \pm 0.025$; once the probe was located at the centreplane, data collection commenced with a 2 min interval of temperature measurements recorded at 50 kHz. A 2 min collection period corresponds to the passage of approximately 80 large-scale (long-wavelength) plumes, ensuring statistical convergence (Wilson & Andrews 2002; Ramaprabhu & Andrews 2004*a*).

4.1.3. *Evolution of the probability distribution function, variance and kurtosis of volume fraction fluctuations*

The initial density fluctuations were measured by positioning the thermocouple at a distance $x = 0.5$ cm downstream from the splitter plate. In addition to measurements at $x = 0.5$ cm, density measurements were also taken at multiple downstream locations at the centreplane of the mixing layer (see table 2) to investigate the evolution of density statistics at various stages of the instability development, including the probability distribution function (PDF), the variance, and the kurtosis of volume fraction fluctuations. In addition, the time-evolution of the density variance spectrum and molecular mixing fraction θ (defined below) were also examined.

The PDF of a measured scalar quantity ϕ is defined discretely by

$$P(\phi) = \frac{F(\phi)}{N_{samp}\, \Delta\phi}, \tag{6}$$

where $F(\phi)$ is the discrete frequency distribution (histogram) of the scalar ϕ, N_{samp} is the number of samples, and $\Delta\phi$ is the bin width of $F(\phi)$. The variance and kurtosis (second- and fourth-order moments) of an ensemble of scalar measurements are

$$\sigma_\phi^2 = \langle \phi'^2 \rangle, \quad K_\phi = \frac{\langle \phi'^4 \rangle}{\langle \phi'^2 \rangle^2}, \tag{7}$$

respectively, where $\phi(x)' = \phi(x) - \langle \phi \rangle$ is the scalar fluctuation. The variance of the volume fraction fluctuations is a measure of the spread of volume fraction values away from the mean value $\langle f_1 \rangle = 0.5$, whereas the kurtosis is a measure of the sharpness of the volume fraction PDF. Kurtosis values of $K_{f_1} < 1.8$ indicate a bimodal distribution with peaks at $f_1 = 0$ and $f_1 = 1$, whereas a value of $K_{f_1} > 1.8$ corresponds to a centrally-peaked PDF, in this case at $\langle f_1 \rangle = 0.5$ (a Gaussian distribution has

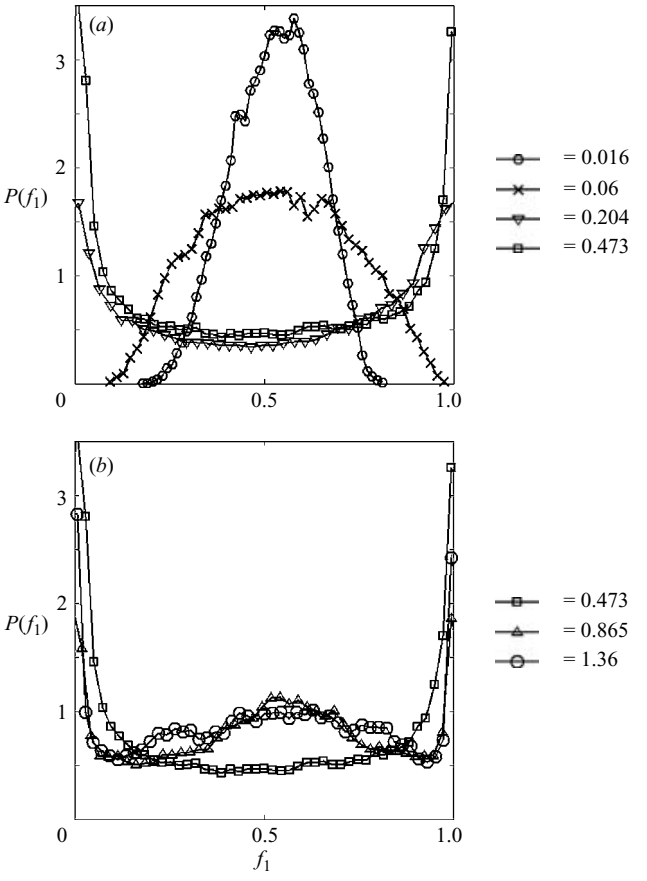

FIGURE 3. Time-evolution of (*a*) the early-time and (*b*) late-time heavy-fluid volume fraction PDF $P(f_1)$ on the centreplane of the mixing layer.

a value $K_{f_1} = 3$). The skewness (normalized third-order moment) of the density fluctuations was measured to be approximately zero on the centreplane, consistent with the expected symmetry of $P(f_1)$ in this small-Atwood-number experiment, and is not discussed further.

Figure 3 shows both the early and intermediate time-evolution of $P(f_1)$. At early times ($\tau = 0.016$ and 0.06), the volume fraction distributions peak at $f_1 = 1/2$, indicating that most of the fluid at the centreline is mixed. However, as the initial bubbles and spikes grow ($\tau = 0.204$ and 0.473), a large portion of the centreplane becomes occupied by pockets of pure hot and cold water engulfed by the mixing layer, causing the distribution to become strongly bimodal. This trend is reversed at later times ($\tau > 0.473$), as a central peak re-emerges in the distribution of $P(f_1)$ as τ and the Reynolds number increase. Similar volume fraction distributions were reported by Ramaprabhu & Andrews (2004*a*) using lower-resolution thermocouples; however, a greater degree of bimodality is reported here. The present measurement refines the measurements reported by Ramaprabhu & Andrews (2004*a*), as smaller thermocouples were used to better resolve the sharp density gradients present during the early stages of mixing (Mueschke & Andrews 2006).

The time-evolution of K_{f_1} (figure 4) quantifies the modality observed in figure 3. The initial single-mode distribution of $P(f_1)$ evolves to a bimodal distribution, and

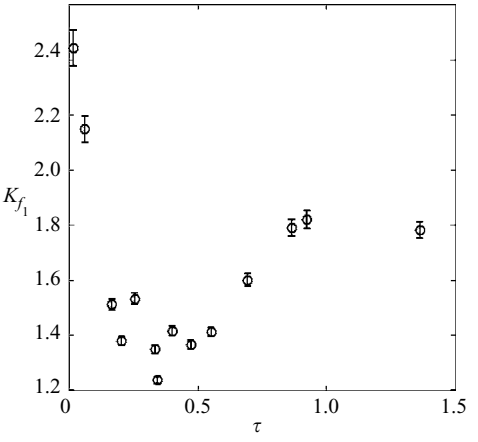

FIGURE 4. Time-evolution of the volume fraction kurtosis on the centreplane.

the values of $K_{f_1}(\tau)$ correspondingly decrease below 1.8. This indicates a strong segregation of the two fluids at early and intermediate times $0.204 < \tau < 0.473$. As nonlinear interactions become increasingly dominant, the range of scales continues to increase, as do the associated interfacial areas between pockets of hot and cold fluid. Thus, as the rate of molecular diffusion increases, so does the value of K_{f_1}.

4.1.4. *The degree of molecular mixing*

Measured density data were also used to determine an integral measure of the degree of molecular mixing $\theta(\tau)$ for a given downstream location. All molecular mixing measurements have been taken at the centreplane of the mixing layer ($z = 0$), and thus do not represent the degree of molecular mixing over the entire mixing-layer width. The measure of molecular mixing used here was first introduced by Dankwerts (1952) as the degree of fluid segregation, and has been used by various workers in a variety of forms (Youngs 1984; Dalziel *et al.* 1999; Wilson & Andrews 2002; Cook *et al.* 2004). The present definition of θ requires two quantities, B_0 and B_2:

$$B_0 \equiv \sigma_{f_1}^2 = \frac{\langle \rho'^2 \rangle}{(\Delta\rho)^2} \tag{8}$$

is the dimensionless variance of density fluctuations corresponding to two miscible fluids at a given downstream location, and

$$B_2 = \langle f_1 \rangle \langle f_2 \rangle = \langle f_1 \rangle (1 - \langle f_1 \rangle) \tag{9}$$

is the dimensionless variance of density fluctuations corresponding to two immiscible fluids (i.e. a pure two-fluid mixture) at a given downstream location, and is readily obtained from (8). The molecular mixing fraction at a given downstream location is then defined as

$$\theta(\tau) = 1 - \frac{B_0(\tau)}{B_2(\tau)}, \tag{10}$$

such that $\theta = 0$ when the two fluids are completely segregated, and $\theta = 1$ when they are completely molecularly mixed (i.e. when the density is uniform). The time-evolution of the centreplane values of B_0, B_2 and θ are shown in figure 5. All measurements were taken at the centreplane of the mixing layer where $\langle f_1 \rangle = 0.5$ and $\langle f_2 \rangle = 0.5$, so

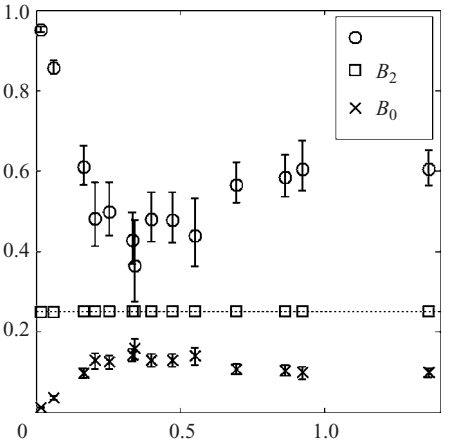

FIGURE 5. Time-evolution of the molecular mixing quantities B_0, B_2 and θ on the centreplane. The values of B_2 all approach a value of 0.25 (dotted line), indicating that the measurements were taken at the centreplane of the mixing layer. The error bars on the measurements are also shown.

that $B_2 = \langle f_1 \rangle \langle f_2 \rangle = 0.25$. A fiducial (dotted line) is shown in figure 5 at a value of 0.25, confirming that all measurement points were taken on the centreplane.

Figure 5 reveals two stages of evolution of the molecular mixing fraction θ. At early times ($\tau < 0.4$), θ decreases rapidly, which occurs during the early-time linear and weakly nonlinear growth of the initial perturbations. The second stage is characterized by an increase in θ ($\tau > 0.4$). The evolution of θ suggests the following dynamical interpretation. A decrease in θ during the first stage is attributed to the initial growth of Rayleigh–Taylor unstable perturbations, leading to a straining of the initial density interface shed from the splitter plate. At the centreplane, the two fluids are 'stirred' with little molecular mixing. A subsequent increase of θ during the second stage is due to the flow complexity associated with the development of strong nonlinearities. Secondary Kelvin–Helmholtz instabilities develop between rising bubbles and falling spikes, rapidly increasing the interfacial area between the fluids and the associated molecular diffusion. This transition is observed in the water-channel experiments at $\tau \approx 0.4$, at which time θ attains its minimum value. Ristorcelli & Clark (2004) noted similar behaviour in a direct numerical simulation of a small-Atwood-number, miscible Rayleigh–Taylor instability-driven mixing layer.

In the present experiment, the degree of molecular mixing at the centreplane of the mixing layer varies significantly over the measurement times $0.016 \leqslant \tau \leqslant 1.36$. The time-evolution of the volume fraction PDF, volume fraction variance and kurtosis, and molecular mixing fraction is shown in figures 3–5, which indicate the same early-time imbalance between the rates of fluid engulfment and molecular mixing. The term *engulfment* is used here in analogy with the term *entrainment*, typically used in shear layers in which the physical mechanism by which fluid enters the mixing layer is different from that in a Rayleigh–Taylor instability-driven mixing layer. Comparison of figures 3–5 at $\tau \approx 0.4$ shows an early-time transition point in the development of the mixing layer when the rates of fluid engulfment and molecular mixing are comparable. Prior to the onset of strong nonlinearity, the growth of the initial buoyant structures engulfs unmixed fluid into the mixing layer before developing substantial surface area

between the two fluids, thereby limiting the amount of molecular mixing. Beyond this transition point, the rate of molecular mixing due to turbulent fluctuations is greater throughout the mixing layer and, as a result, both the rate of molecular mixing and the amount of mixed fluid at the centreplane increase.

The molecular mixing between two fluids in a miscible Rayleigh–Taylor mixing layer is difficult to measure owing to the large number of samples required for the statistical convergence of $\langle f_1 \rangle$ and $\sigma_{f_1}^2$, with the measurement points taken with sufficient spatial resolution to resolve all density gradients (Mueschke & Andrews 2006). Other workers have typically reported values of $\theta(z)$ across the mixing layer or of $\Theta(\tau)$ (a global measure of molecular mixing) for late times (Youngs 1991), rather than the evolution of $\theta(z=0, \tau)$, as reported here. Ramaprabhu & Andrews (2004*a*) also measured $\theta(z=0, \tau)$ in the same water channel as used in the present investigation. In the present work, a minimum value of $\theta \approx 0.4$ was measured and occurs at the same time $\tau \approx 0.4$ as in Ramaprabhu & Andrews (2004*a*), but is lower than their reported value $\theta = 0.68$. The difference between the measured values of θ reported here and by Ramaprabhu & Andrews (2004*a*) is attributed to the difference in the size of the thermocouple probes and to the noise elimination techniques used in the present work (Mueschke 2004; Mueschke & Andrews 2006). Ristorcelli & Clark (2004) report a similar two-stage behaviour of $\theta(z=0, \tau)$; however, the exact time of transition and the minimum value of θ differ. The difference between the present early-time measured results and the simulation results of Ristorcelli & Clark may be because the initial velocity field was zero in the numerical simulations.

4.1.5. *Evolution of the density variance spectrum*

Consider the time-evolution of the density variance spectrum. The amplitudes of the density fluctuations are given by the one-dimensional Fourier transform

$$\hat{\rho}(k, \tau) = \frac{2}{L} \int_0^L \rho(x, \tau) \mathrm{e}^{-\mathrm{i}kx} \, \mathrm{d}x, \tag{11}$$

where $k \equiv 2\pi/\lambda$ is the wavenumber corresponding to wavelength λ and L is the distance over which $\rho(x)$ was measured (see equation (5)). The change from temporal variation to spatial variation uses Taylor's hypothesis to relate $\rho(t)$ and $\rho(x)$ (Pope 2000). As the probe volume records pointwise measurements, the dependence of the density field upon the other spatial and temporal dimensions is suppressed for brevity. The complex-valued amplitude and phase is given by (11), from which the one-dimensional energy spectrum is

$$E_{\rho}(k, \tau) = \frac{\hat{\rho}(k, \tau)^* \, \hat{\rho}(k, \tau)}{4\Delta k}, \tag{12}$$

where $\hat{\rho}^*$ is the complex conjugate of $\hat{\rho}$ and $\Delta k = 2\pi/L$ is the wavenumber bin width. It follows that

$$\frac{\langle \rho'^2 \rangle(\tau)}{2} = \int_0^{\infty} E_{\rho}(k, \tau) \, \mathrm{d}k \tag{13}$$

in the continuum wavenumber limit.

In general, density variance spectra calculated from pointwise measurements are noisy for several reasons, including the finite recording time of data points and random errors due to electronic noise. The fluctuations in $E_{\rho}(k, \tau)$ render it difficult to estimate accurately the spectral slopes in various power-law regimes. In order to elucidate possible scaling laws of the density variance spectra, the original spectra

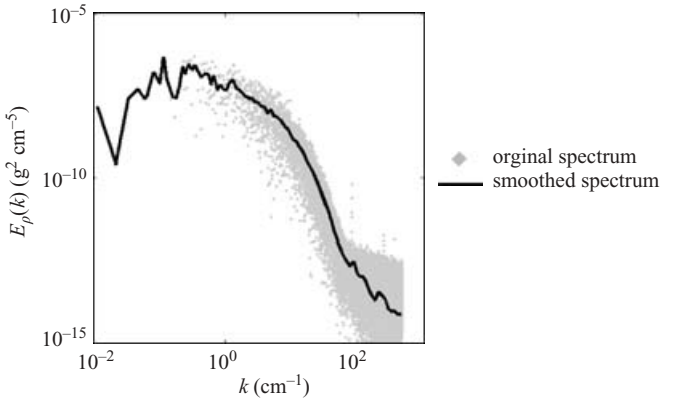

FIGURE 6. Illustration of a smoothed density variance spectrum using the logarithmic binning procedure.

must be smoothed. Ramaprabhu & Andrews (2004*a*) used a Savitsky–Golay filtering technique, which fits an nth-order polynomial to a moving window ($2n+1$ points wide) to perform smoothing. However, significant filtering is required to smooth the intermediate-to-large wavenumber variance spectra. The present study further improves upon this by implementing a smoothing procedure that conserves energy in local wavenumber regions by binning variance values into wavenumber bins, Δk, which increase in size logarithmically. This method is conservative by construction and significantly smoothes the intermediate- and large-wavenumber modes. As in standard discrete sampling theory, the density variance spectrum $E_\rho(k,\tau)$ is originally sorted in wavenumber bins of constant size $\Delta k = 2\pi/L$. To smooth the spectra, the density variance per unit wavenumber from (12) was apportioned into wavenumber bins logarithmically increasing in size and normalized by the local wavenumber bin width: this results in a procedure that averages the density variance over a wavenumber bin width that increases in size at the same rate as the number of modes resolved at larger wavenumbers. This procedure conserves the energy content of the spectrum, which was confirmed by comparing the integrals of the original spectra with those of the smoothed spectra. Figure 6 illustrates the results of the smoothing procedure by plotting the unsmoothed and smoothed spectra.

Another characteristic of experimentally measured variance spectra is the horizontal 'tail' at large wavenumbers, indicating the level at which the system noise is greater than the measured fluctuations. It is possible to improve the dynamic range of $E_\rho(k,\tau)$ measured by subtracting the system noise from the measured density variance spectrum using Wiener filtering (Press *et al.* 2002), requiring either an estimate or a measurement of the noise. In the present work, the background noise was measured by filling the channel with water and allowing thermal equilibrium to be attained. A thermocouple probe was placed in the water channel and a 2 min sample of the background noise was measured at 50 kHz. Fluctuations in the temperature induced by EMF and RFI noise were converted to density using (3). The variance spectrum of the background noise was then calculated and subtracted from the measured density variance spectrum. This procedure provided an additional decade of measurable values at the largest wavenumbers. The subtraction of the background noise also eliminated a large portion of spurious noise from the initial density variance spectrum at $\tau = 0.016$, which will be discussed in detail next.

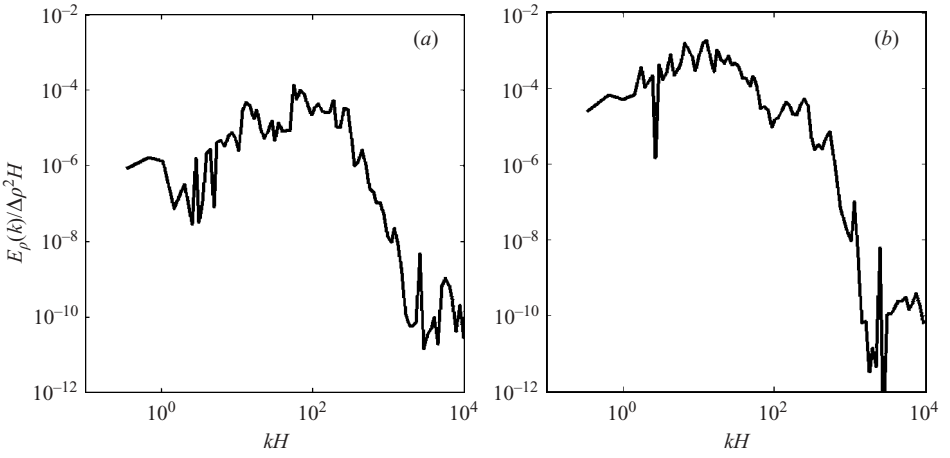

FIGURE 7. The normalized density variance spectrum at (*a*) $\tau = 0.016$ or at $x = 0.5$ cm downstream and (*b*) $\tau = 0.06$ or at $x = 2.0$ cm downstream.

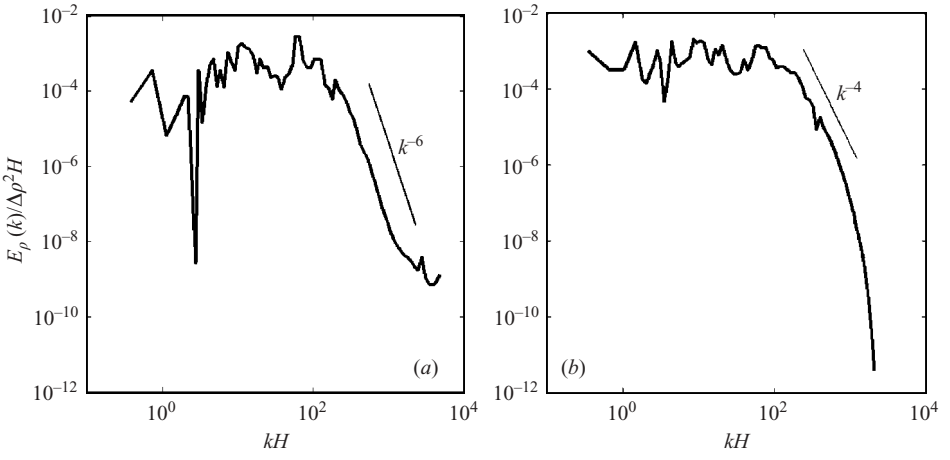

FIGURE 8. The normalized density variance spectrum at (*a*) $\tau = 0.204$ or at $x = 6.0$ cm downstream and (*b*) $\tau = 0.473$ or at $x = 15.0$ cm downstream.

The early-time density variance spectra ($\tau = 0.016$) shown in figure 7 exhibit broadbanded perturbations at the onset of the instability. However, the density variance spectrum at $\tau = 0.06$ contains considerably more energy in the non-dimensional wavenumber range $kH < 100$; it is hypothesized that the initial perturbations in the streamwise direction are driven by vertical velocity fluctuations. The relationship between the initial density variance spectrum and the vertical velocity variance spectrum near the edge of the splitter plate will be further discussed in § 4.1.6. While the early-time ($\tau = 0.016$) spectra exhibit broadbanded energy content, the majority of the energy is contained near the peak value of $kH \approx 90$. The peak variance value is two orders of magnitude greater than the longest wavelength content of the spectrum. Relating the energy content to the amplitude of the perturbation, $\|\hat{\rho}(k,\tau)\| \sim \sqrt{\langle \rho'^2 \rangle(k,\tau)}$, yields a ratio of peak perturbation amplitude to long-wavelength perturbation amplitude of $\hat{\rho}_{peak}/\hat{\rho}_{kH<10} \approx 10$. Thus, while the experiment contains longer wavelengths in the initial density spectrum, the amplitudes of these

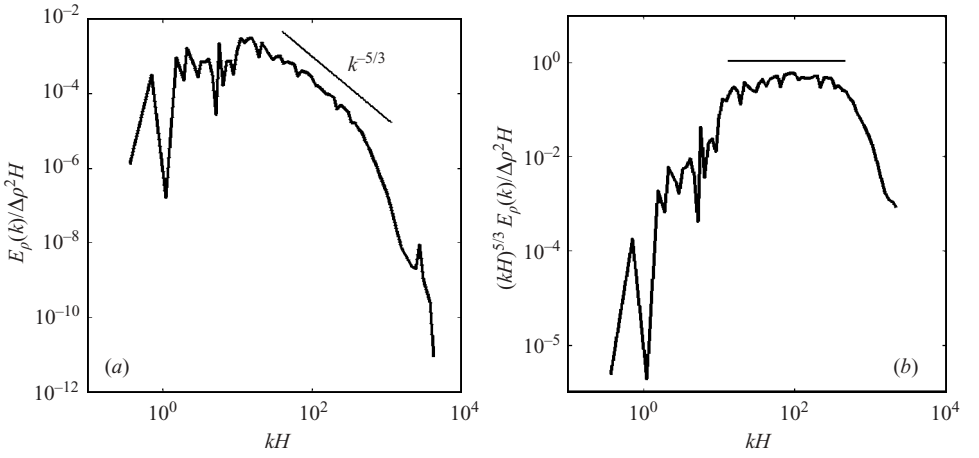

FIGURE 9. The normalized density variance spectrum at (*a*) $\tau = 0.865$ or at $x = 25.0\,\mathrm{cm}$ downstream; (*b*) the compensated spectrum at $\tau = 0.865$ indicates a short range of apparent $k^{-5/3}$ scaling.

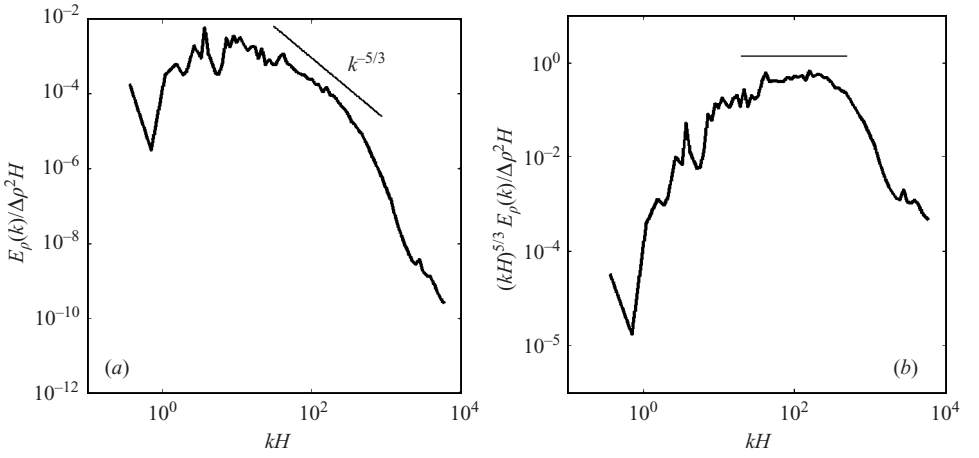

FIGURE 10. The normalized density variance spectrum at (*a*) $\tau = 1.36$ or at $x = 40.0\,\mathrm{cm}$ downstream; (*b*) the compensated spectrum at $\tau = 1.36$ indicates a short range of apparent $k^{-5/3}$ scaling.

long-wavelength perturbations are much smaller than those of the intermediate wavelength perturbations, and are believed to contribute insignificantly to the early transitional dynamics of the mixing layer. However, any implementation of the initial conditions in a numerical simulation should retain this small-wavenumber energy content, as longer wavelength perturbations have been shown to be important in the late-time dynamics of a Rayleigh–Taylor unstable mixing layer (Linden *et al.* 1994; Dimonte 2004; Dimonte *et al.* 2005).

As the mixing layer develops, a steep decay in the energy spectrum is noted at larger non-dimensional wavenumbers ($kH > 100$) as small-scale fluctuations are damped by diffusion (figure 8). However, definitive power-law scalings are difficult to determine because of the short interval over which the decay occurs (less than one decade). At later times ($\tau = 0.865$ and 1.36), a small range of scales exhibit an approximate

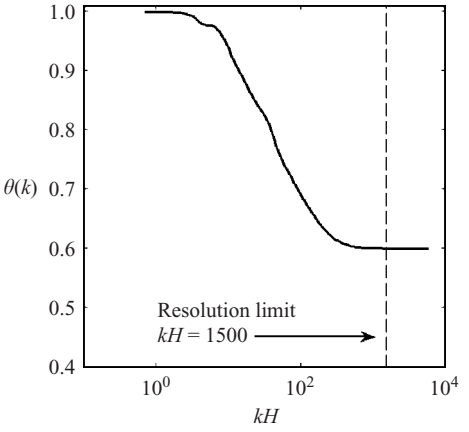

FIGURE 11. Spectral molecular mixing fraction $\theta(k)$ versus dimensionless wavenumber at $\tau = 1.36$.

$k^{-5/3}$ scaling, (figures 9 and 10). Compensated density variance spectra are shown in figures 9 and 10 as well, with an apparent inertial subrange over approximately one decade of wavenumbers. The slight deviation may be due to the limited Reynolds numbers attained in the experiment: Ramaprabhu & Andrews (2004*a*) also estimated the integral-scale Reynolds number $Re \approx 1000$–1450 at $\tau = 1.21$, depending upon the choice of length scale L and velocity-scale U. Wilson & Andrews (2002) and Ramaprabhu & Andrews (2004*a*) reported a late-time $k^{-5/3}$ scaling. They also showed that an inertial subrange for $E_\rho(k, \tau)$ exists over approximately one decade of wavenumbers at $\tau = 2.08$, consistent with the current results.

An accurate measure of the density variance spectrum and of the molecular mixing fraction θ requires measurement times sufficient for statistical convergence of the larger scales, while adequately resolving the small-scale structures. As given in § 4.1.1, the frequency response of the thermocouple probe is 71 Hz or $kH \approx 1500$, depending upon the exact mean flow velocity. Ramaprabhu & Andrews (2004*a*) estimated $Re = 1250$ at $\tau = 1.21$, resulting in a Kolmogorov scale $\eta_K = h_b Re^{-3/4} = 0.29$ mm ($kH = 6900$) and a Batchelor scale $\eta_B = \eta_K Pr^{-1/2} = 0.11$ mm ($kH = 18\,300$). Thus, the thermocouple measurement system is not capable of resolving approximately the final decade of wavenumbers in the dissipation subrange of the density variance spectrum. However, the error introduced by not resolving this final decade can be shown to be negligible. For example, taking $B_2 = 0.25$ at the centreplane (by definition) and substituting (8) and (13) into (10), θ can be written in terms of the density variance spectrum:

$$\theta(\tau) = 1 - \frac{8}{(\Delta\rho)^2} \int_0^\infty E_\rho(k, \tau)\, \mathrm{d}k. \tag{14}$$

To examine the integral contribution of higher-wavenumber density fluctuations to θ, consider the spectral molecular mixing fraction

$$\theta(k, \tau) = 1 - \frac{8}{(\Delta\rho)^2} \int_0^k E_\rho(k', \tau)\, \mathrm{d}k'. \tag{15}$$

As additional wavenumbers are included in the integration of the measured $E_\rho(k, \tau)$, $\theta(k, \tau)$ converges to $\theta(\tau)$, as shown in figure 11. This result demonstrates that the majority of the energy content is in the smaller wavenumbers of the spectrum.

Experiment	Physical window size (cm)	Final interrogation window (pixels)	Spatial resolution (cm)
Non-buoyant ($A = 0$)	4.44×3.33	32×32	0.22
Rayleigh–Taylor ($A \approx 7 \times 10^{-4}$)	5.33×4.00	32×32	0.27

TABLE 3. PIV diagnostic parameters in a typical experiment.

The same conclusion was reached by Wilson & Andrews (2002) by examining the cumulative energy distribution of density fluctuations. More importantly, $\theta(k, \tau)$ attains the asymptotic value of $\theta(\tau)$ before the measurement resolution limit $kH = 1500$. Thus, the additional decade of energy in the dissipation range beyond the resolution limit of the probe can be assumed negligible in terms of the measurement of $\theta(\tau)$ for the mixing layer and Prandtl number considered here.

4.2. *PIV diagnostics and measurements of streamwise velocity perturbations*

4.2.1. *Description of the PIV system*

Velocity perturbations in the streamwise direction were measured using particle-image velocimetry (PIV) (Adrian 1991, 2005). The PIV system consisted of two 120 mJ Nd-YAG lasers (532 nm), each with a firing rate of 15 Hz and a pulse width of 5 ns. The lasers were triggered in an alternating fashion, resulting in an effective 30 Hz sampling rate. Each 500 gallon water tank was seeded with 3.5 g of Conduct-O-Fil® silver-coated hollow glass spheres having a mean particle diameter $D_p = 13\,\mu$m and density $\rho_p = 1.6\,\mathrm{g\,cm^{-3}}$. The ability of a particle to follow a given flow field can be measured by the particle Stokes number

$$St = \frac{\tau_p}{\tau_f}, \tag{16}$$

where τ_p and τ_f are the particle and flow-field time scales, respectively (Adrian 1991; Fallon & Rogers 2002). For $St \ll 1$, the particle paths are capable of tracking the streamlines of the flow. The time scale of a spherical particle is typically defined as

$$\tau_p = \frac{\rho_p D_p^2}{18\mu}, \tag{17}$$

where μ is the dynamic viscosity of the fluid. The flow-field time scale is chosen to be the Kolmogorov time scale $\tau_f = \tau_\eta = 0.084$ s at $\tau = 0.92$ ($x = 27$ cm), as it is the turbulent scale that contains the highest vorticity gradients and is the most difficult for the particles to track (Fallon & Rogers 2002). Accordingly, $St = 0.017 \ll 1$ for the highest Reynolds numbers attained in the current experiments, making the particles well-suited for these experiments. A series of cylindrical lenses created a sheet of laser light in the (x, z)-plane of the water channel (figures 1 and 12). The laser sheet was positioned so that the u and w (streamwise and vertical) components of the velocity field were measured in a plane just off of the splitter plate, near its midspan. The measurements of u and w were then decomposed into their mean ($\langle u \rangle$ and $\langle w \rangle$) and fluctuating (u' and w') components.

Images were captured using a Kodak *Megaplus*™ digital imaging system. The image-capturing system and laser triggering system were synchronized using a pulse generator (Kraft 2004). A series of 1200 images with a resolution of 640×480 pixels was recorded using *LabVIEW*™. The spatial resolutions of the PIV measurements are given in table 3. Instantaneous velocity fields were determined by calculating the

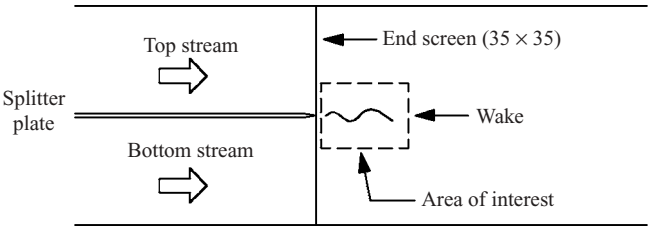

FIGURE 12. Schematic of the domain measured by the PIV system in the water channel.

two-dimensional cross-correlation of two successive images using *MATPIV* (Grue *et al.* 2000; Sveen 2004). Particle displacement vectors were calculated from the cross-correlation of an interrogation window within two successive images:

$$R(x,\ y) = \sum_{i=-M/2}^{M/2} \sum_{j=-N/2}^{N/2} I_1(i,\ j) I_2(i+x,\ j+y), \tag{18}$$

where I_1 and I_2 are the two-dimensional 8-bit scalar intensity fields recorded by the image-capturing system. The particle displacement vector is the distance between the centre of the interrogation window and the peak of the cross-correlation function in two-dimensional space. Displacement vectors outside of two standard deviations from their neighbours were discarded and replaced by interpolated values. The *MATPIV* post-processing algorithm employed a multi-pass technique, in which the initial pass operated on 64×64 pixel interrogation windows. The second pass used displacement vectors from the first pass as initial estimates for 32×32 pixel interrogation windows. In both the first and second passes, the interrogation windows overlapped by 50%, resulting in a final field of 39×29 velocity vectors. To examine the velocity fluctuations at a given point in space, the u and w velocity components at a given (x, z) location were taken from each of the 1199 velocity fields. The uncertainty in the velocity measurements was determined by Ramaprabhu (2003) to be $\pm 0.05\,\mathrm{cm\,s^{-1}}$ using standard methods described by Adrian (1997). The variance of the second moments $\langle u'^2 \rangle$ and $\langle w'^2 \rangle$ were estimated such that

$$S_{\langle \phi'^2 \rangle} \cong \frac{\sqrt{\langle \phi'^4 \rangle - \langle \phi'^2 \rangle^2}}{N_{samp} \langle \phi'^2 \rangle}, \tag{19}$$

where $N_{samp} = 1199$ for PIV measurements (Benedict & Gould 1996). The estimated uncertainty was calculated using a 95 % confidence interval, where the uncertainty is $\pm 1.96\, S^{1/2}_{\langle \phi'^2 \rangle}$. The relative uncertainty in the horizontal and vertical velocity variances are $\langle u'^2 \rangle = \pm 4.5\,\%$ and $\langle w'^2 \rangle = \pm 3.0\,\%$ at $\tau \approx 0.9$. This represents a conservative error estimate, as these estimates were calculated at the furthest downstream location measured, i.e. the fewest large-scale structures were observed during the 40 s capture time interval.

4.2.2. *Measurement of the initial velocity perturbations at the interface*

To quantify the initial velocity perturbations at the two-fluid (hot and cold water) interface, PIV measurements were performed in the wake immediately following the trailing edge of the splitter plate and end-screen (0.4–4.0 cm), as shown in figure 12. Velocity measurements were taken with no temperature difference between the two streams, so that the momentum disturbance generated by the experimental apparatus

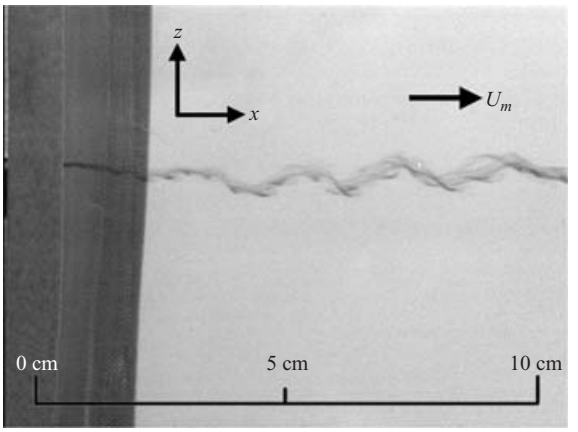

FIGURE 13. Photograph of Nigrosene dye streakline shedding from the splitter plate.

could be isolated from the Rayleigh–Taylor unstable configuration. It is proposed that the mean and fluctuating velocity field trailing the splitter plate is one of a laminar vortex sheet, where the vertical velocity fluctuations measured in the wake of the plate result from the separating boundary layers above and below the plate. To visualize the flow field in the wake of the splitter plate, Nigrosene dye was injected onto the surface of the plate, upstream of the trailing edge. Figure 13 shows a typical photograph of the dye streakline, which exhibits a periodic structure similar to that of a wake-shedding flow. Small variations in the dye streak are attributed to non-uniform dye injection and perturbations imposed by the end-screen. A conservative estimate of the wake Reynolds number behind the splitter plate is $Re \approx 152$, based on the mean velocity and plate thickness. This estimate represents an upper bound, as it does not account for the knife-edge at the end of the splitter plate. The structures in figure 13 do not exhibit the structure or roll-up typical of wakes with $Re \approx 150$. For this reason, the actual wake Reynolds number is probably closer to the lower-bound limit of $Re = 49$, where the wake initially becomes unsteady (Williamson 1996). Furthermore, the upper-bound wake Reynolds number is below the threshold of $Re = 194$, where wakes begin to exhibit three-dimensional structure. Accordingly, spanwise velocity fluctuations are not expected in the initial conditions of this experiment. More details on the spanwise perturbations are given in § 4.3.

A contour plot of the vertical fluctuating velocity variance $\langle w'^2 \rangle$ in the region following the splitter plate is shown in figure 14, where a small wake behind the splitter plate is visible in the peak values of $\langle w'^2 \rangle$ (white in the figure). Figure 15 shows the evolution of $\langle w'^2 \rangle$ at the centreline of the wake. Equations (11) and (12) are used in a similar manner to calculate $\hat{w}(k, \tau)$ and $E_w(k, \tau)$. The vertical velocity variance spectrum at $x = 1.0$ cm downstream ($\tau \approx 0.03$) is shown in figure 16, and can be quantitatively related to the dye streak image shown in figure 13. The approximate wavelength of the structures shed from the splitter plate is $\lambda \approx 2.5$ cm ($k \equiv 2\pi/\lambda \approx 2.5\,\mathrm{cm}^{-1}$), as measured from figure 13. The wavenumber of the shedding structures measured from the streaklines matches the wavenumber of the peak of the initial vertical velocity variance spectrum (figure 16).

The initial vertical velocity variance spectrum can also be qualitatively related to the early-time density variance spectra shown in figure 7. The density variance spectrum (figure 7) at $\tau = 0.016$ exhibits two local maxima at approximately $kH \approx 12$

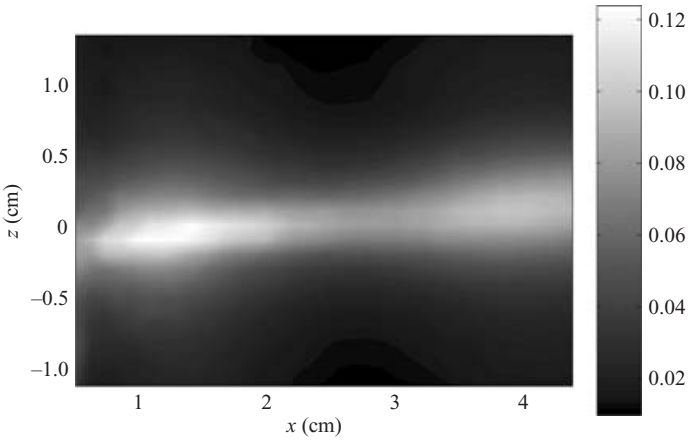

FIGURE 14. Field of the vertical velocity variance $\langle w'^2 \rangle$ at downstream locations $x = 0.5$–4.0 cm.

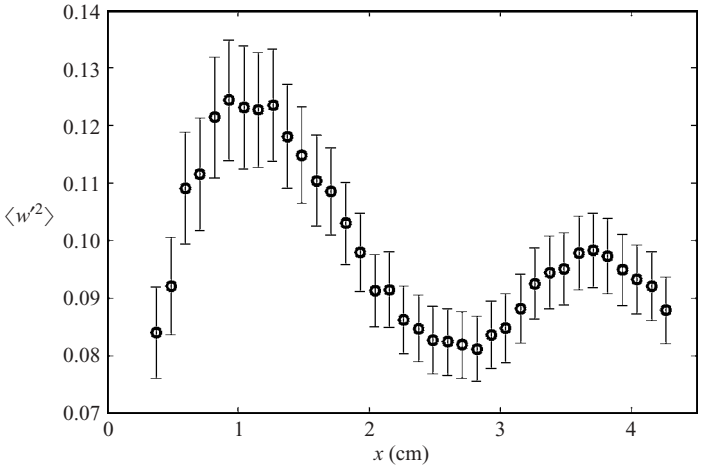

FIGURE 15. Early-time decay of $\langle w'^2 \rangle$ at downstream locations $x = 0.5$–4.0 cm following the trailing edge of the splitter plate with the channel in a non-buoyant configuration. The error bars on the measurements are also shown.

($\lambda \approx 16.7$ cm) and at $kH \approx 90$ ($\lambda \approx 2.2$ cm). The vertical velocity variance spectrum (figure 16) also exhibits two local maxima at $k \approx 0.4\,\mathrm{cm}^{-1}$ ($\lambda \approx 15.7$ cm) and at $k \approx 3\,\mathrm{cm}^{-1}$ ($\lambda \approx 2.1$ cm). It is evident that the two peaks in the density variance and velocity variance spectra occur at similar wavelengths. It is also noted that the longer wavelength ($\lambda \approx 16$ cm) perturbations are less pronounced than the shorter wavelength ($\lambda \approx 2.1$ cm) perturbations. This correlation between the peaks of the vertical velocity and density variance spectra suggests that the wake shedding behind the splitter plate, and hence the initial velocity fluctuations, predominantly influence the early-time ($\tau < 0.2$) development of the mixing layer.

In addition to comparing the peaks of the velocity and density variance spectra, it is possible to examine the rate at which energy, $\langle w'^2 \rangle/2$ and $\langle \rho'^2 \rangle/2$, evolve across a spectrum of modes in order to study the early-time evolution of the mixing layer. By

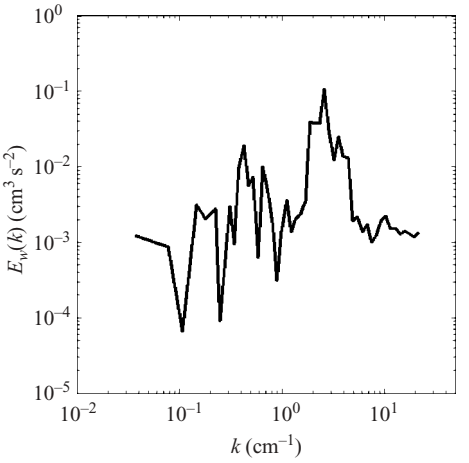

FIGURE 16. The vertical velocity variance spectrum at a distance $x = 1.0$ cm from the splitter plate.

examining the early-time evolution of $E_\rho(k)$ (see figure 7) it is observed that a large percentage of the change in $E_\rho(k, \tau)$ from $\tau = 0.016$ to 0.06 occurs in the smallest wavenumbers ($kH < 50$). From linear stability analysis of a Rayleigh–Taylor unstable interface including viscous effects, the most unstable wavelength is

$$\lambda_m \approx 4\pi \left(\frac{\nu^2}{A\, g} \right)^{1/3} \tag{20}$$

(Chandrasekhar 1961). Taking the kinematic viscosity of the mixture $\nu = (\mu_1 + \mu_2)/(\rho_1 + \rho_2)$ and $A = 7.5 \times 10^{-4}$, the most unstable wavelength is $\lambda_m = 0.65$ cm, corresponding to $kH \approx 311\ \text{cm}^{-1}$. Linear stability analysis indicates that, in the absence of external forces and velocity fields, the large wavenumber density variance spectrum (near $kH \approx 311$) should accumulate energy at the greatest rate, and the exponential growth and accumulation of energy at wavenumbers $kH \ll 311$ should be small. However, the largest change in the density variance spectrum between $\tau = 0.016$ and 0.06 is observed in the smaller wavenumbers ($1 < kH < 100$). This early-time growth is attributed to the velocity-perturbation-driven growth of the mixing layer in the wake of the splitter plate ($\tau < 0.2$), where the initial velocity spectrum exhibits the majority of its energy content in the smaller wavenumbers ($1 < kH < 100$).

While vertical velocity fluctuations are hypothesized to be the dominant mechanism contributing to the initial development of the Rayleigh–Taylor mixing layer in the experiment, the current set of measurements allows second-order effects at $\tau \approx 0$ to be measured as well, such as the velocity deficit in the wake trailing the splitter plate. A contour plot of $\langle u \rangle$ is shown in figure 17, and the decrease in U_m (velocity deficit) at the edge of the splitter plate is evident. The slight drift of the mixing-layer centreplane, as discussed in § 4.1.2, can be seen in the slight rise of the velocity mean deficit in figure 17. Again, nothing was observed or measured to indicate that this slight drift affected the results presented here.

Ramaprabhu (2003) reported a velocity deficit of $\approx 10\,\%$ of the mean advection velocity at a distance $x = 1.0$ cm from the splitter plate. This deficit was found to be negligible at $x = 2.0$ cm, as buoyancy effects began to dominate the mixing-layer dynamics. The current measurements exhibit a 5 % difference between the mean

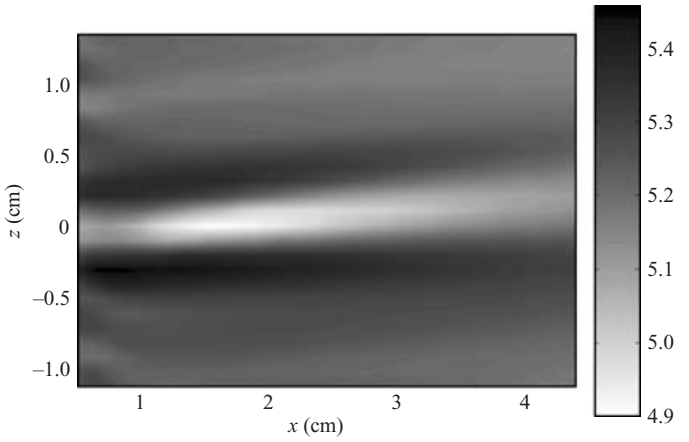

FIGURE 17. Contour of the mean advective velocity $\langle u \rangle \, \mathrm{cm\,s^{-1}}$ in the near wake of the splitter plate (downstream locations $x = 0.5$–$4.0\,\mathrm{cm}$) with the water channel in a non-buoyant configuration.

advection velocity ($U_m = 5.15\,\mathrm{cm\,s^{-1}}$) and the minimum velocity within the wake ($u_{min} = 4.9\,\mathrm{cm\,s^{-1}}$) at $x = 1.0\,\mathrm{cm}$ downstream. This reduction in the velocity deficit behind the splitter plate is attributed to the existence of smaller boundary layers at the knife-edge of the splitter plate, which are a result of modifications to the upstream screen meshes (Mueschke 2004). In addition to the velocity deficit, two thin layers of higher-velocity ($u \approx 5.4\,\mathrm{cm\,s^{-1}}$) fluid exist just above and below the wake of the splitter plate and are probably due to the velocity profile induced by the series of upstream screen meshes. There is no evidence that this mean velocity profile significantly affects the formation of the initial vortex sheet (figures 13–16), or the growth of the mixing layer described in the following section.

4.2.3. *Evolution of velocity variances, probability distribution functions and spectra*

The evolution of the horizontal and vertical velocity variances, $\langle u'^2 \rangle$ and $\langle w'^2 \rangle$, respectively, at the centreplane of the mixing layer was quantified by taking measurements at multiple downstream locations. The evolution of $\langle u'^2 \rangle$ and $\langle w'^2 \rangle$ is shown in figure 18. Small variations in each experimental run account for the range of variance values reported. Both $\langle u'^2 \rangle$ and $\langle w'^2 \rangle$ are initially very small in magnitude, although finite. During the initial development of the mixing layer, vertical velocity fluctuations grow more rapidly than horizontal fluctuations as a consequence of the continual forcing in the gravitational (vertical) direction, with little energy transferred from the vertical to horizontal directions by secondary instabilities and turbulent fluctuations. At $\tau = 0.2$, the ratio of vertical to horizontal velocity variances is approximately $\langle w'^2 \rangle / \langle u'^2 \rangle \approx 5.6$. This ratio remains relatively stationary, where $\langle w'^2 \rangle / \langle u'^2 \rangle \approx 5.8$ at $\tau = 0.5$. However, as turbulent motions and additional three-dimensional structure develops, the ratio decreases slightly to ≈ 4.4 as more energy is contained in the horizontal velocity fluctuations. This ratio can also be seen in the probability density functions of u' and w' (figure 19). The second moments $\langle u'^2 \rangle$ and $\langle w'^2 \rangle$ are a measure of the spread of $P(u')$ and $P(w')$. At each time shown in figure 19, the vertical velocity fluctuations exhibit a much greater range of values.

In addition to the evolution of $\langle u'^2 \rangle$ and $\langle w'^2 \rangle$, the spectral evolution of $E_u(k)$ and $E_w(k)$ at the centreplane are shown in figures 20 and 21. At the earliest times ($\tau = 0.017$ and 0.307), the peak energy values in the vertical velocity fluctuations at

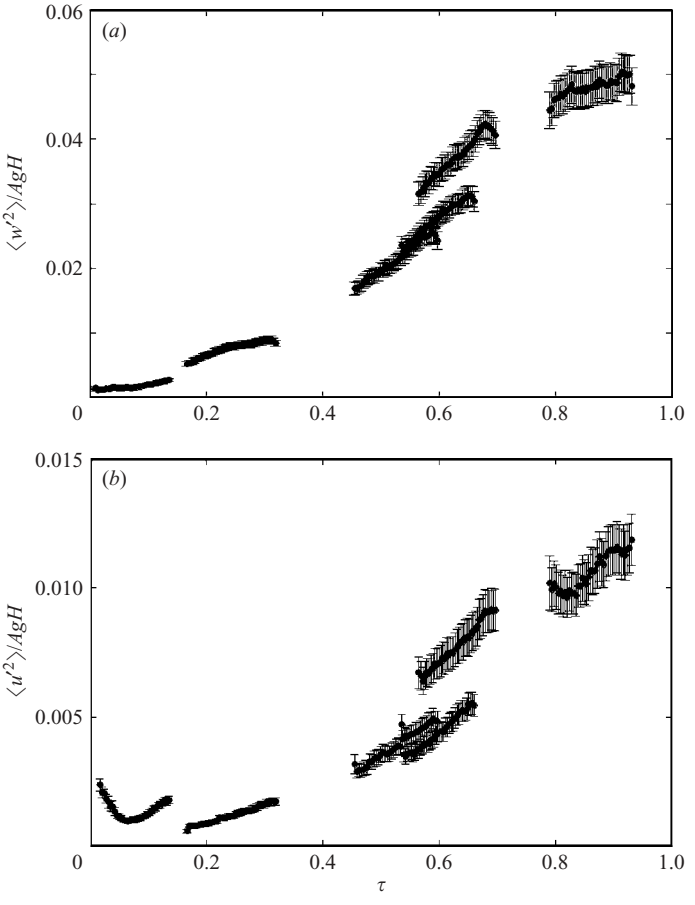

FIGURE 18. Time-evolution of (*a*) the vertical and (*b*) the horizontal normalized velocity variance on the centreplane. The error bars on the measurements are also shown.

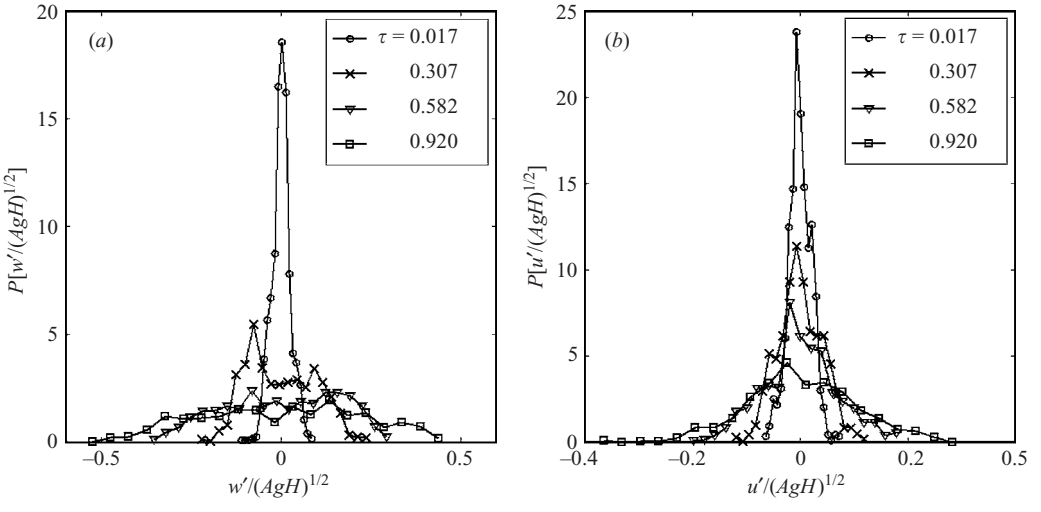

FIGURE 19. Time-evolution of the PDF of (*a*) the vertical and (*b*) the horizontal normalized velocity fluctuations on the centreplane of the mixing layer.

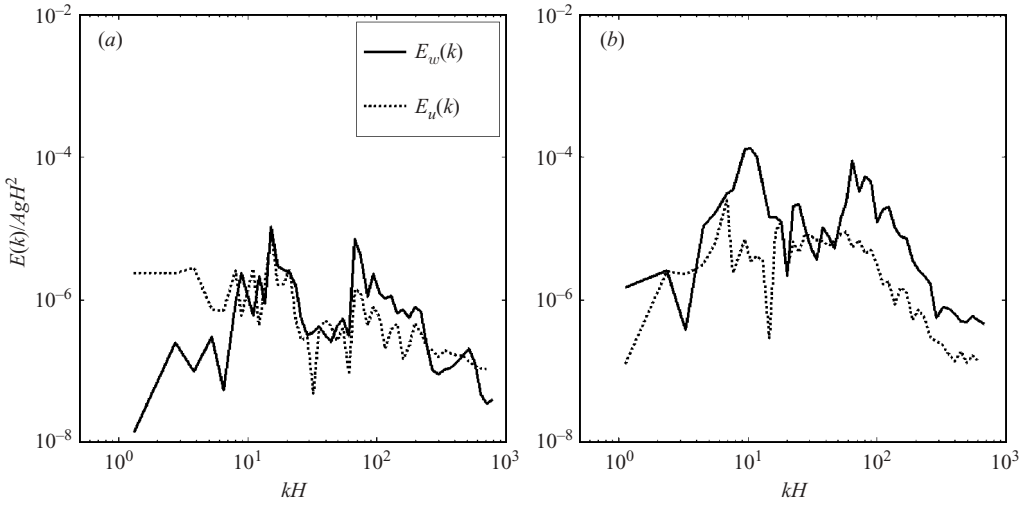

FIGURE 20. The normalized vertical (solid) and streamwise (dashed) velocity variance spectrum at (*a*) $\tau = 0.017$ downstream and (*b*) $\tau = 0.307$ downstream.

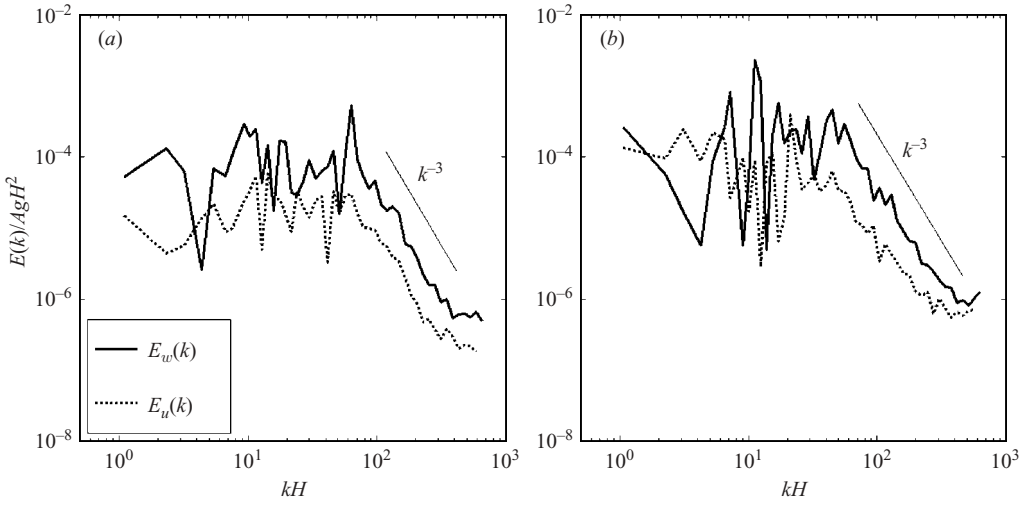

FIGURE 21. The normalized vertical (solid) and streamwise (dashed) velocity variance spectrum at (*a*) $\tau = 0.582$ downstream and (*b*) $\tau = 0.920$ downstream.

$kH \approx 10$ and ≈ 100 can be clearly seen. These peaks correspond to the peak values measured in the non-buoyant arrangement (figure 16). At later times ($\tau = 0.582$ and 0.920), these peaks are no longer distinct features of the spectrum. As the initial dominant modes saturate, nonlinear dynamics result in significant energy transfer to modes above and below the wavenumber peaks at $kH \approx 10$ and ≈ 100. As a cascade of energy to smaller scales develops, an approximate k^{-3} scaling develops at $\tau = 0.582$ and 0.920 (figure 21). This scaling has been noted by previous workers examining Rayleigh–Taylor unstable flows (Wilson 2002; Ramaprabhu & Andrews 2004*a*) and turbulent buoyant plumes (Papanicolaou & List 1987; Dai, Tseng & Faeth 1994; Fisher & Ball 1999). Also, in this larger-wavenumber regime, the vertical velocity

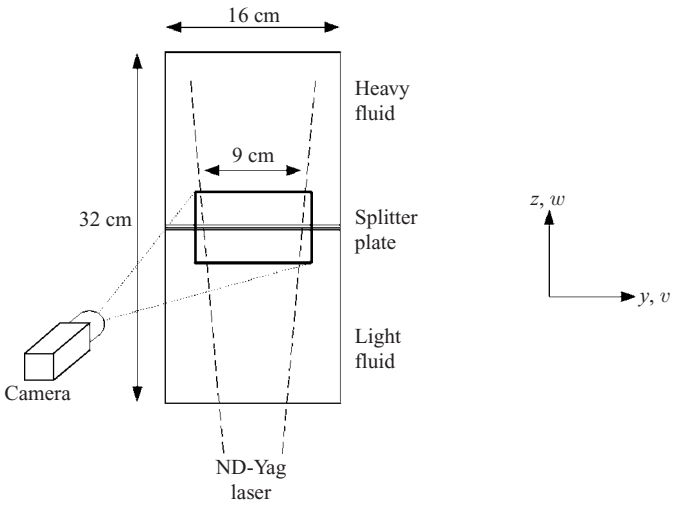

FIGURE 22. Schematic of the experimental laser sheet configuration for the spanwise PLIF measurements.

fluctuations contain almost one order of magnitude more energy than the horizontal fluctuations: this anisotropy persists to the smallest scales measured.

4.3. *PLIF diagnostics and measurements of the spanwise interfacial perturbation*

4.3.1. *Description of the PLIF system*

Planar laser-induced fluorescence (PLIF) was used to measure the interfacial perturbations in the spanwise (y) direction. PLIF detects the presence of a scalar by seeding one fluid stream with a dye that fluoresces when excited by a specific wavelength of laser light (Jacobs 1992; Lee *et al.* 1992). To perform the PLIF measurements, the optical arrangement of the PIV system was modified so that the laser sheet was perpendicular to the mean channel flow. A schematic of the camera and laser sheet arrangement is shown in figure 22. Rhodamine 6G dye (2.5 g) was added to the 500 gallon tank containing the top (cold) stream such that it would fluoresce in the presence of 532 nm laser light. The laser sheet was placed at a distance $x = 0.5$ cm from the trailing edge of the splitter plate so that only the top stream was illuminated, thereby allowing the determination of the two-fluid interfacial perturbation. The digital imaging system used in the thermocouple and PIV experiments was modified to record images of 1000×480 pixels over a domain size of approximately $10\,\text{cm} \times 5\,\text{cm}$. The imaging system was synchronized with the laser system in the same manner as in the PIV configuration (Kraft 2004).

One potential concern with the use of PLIF in the water channel is that the diffusivities of heat and of the fluorescing dye marker are very different. As a temperature difference between the two streams induces the density difference, the two-fluid mixture is miscible, with a Prandtl number $Pr = \nu/D \approx 7$, where ν and D are the kinematic viscosity and thermal diffusivity of water, respectively. However, Rhodamine 6G dye in the top stream diffuses into the bottom stream at a much slower rate than the diffusion of heat (where the Lewis number is $Le \equiv Pr/Sc \sim 10^3$), raising the question of whether the dye is an accurate marker for the two-fluid interface. This error was minimized in the current investigation by taking measurements in the limit of $\tau \to 0$ (i.e. near the splitter plate) such that the difference between the amounts of diffusion is negligible. As there is insufficient time for significant thermal diffusion

to occur, the dye can be regarded as an accurate marker for the cold-water stream. Other than the negligible difference in the diffusion at early times, the location of the two-fluid interface is the only information obtained from the measurement, rather than data pertaining to the internal flow structure. For this reason, no calibration was required to correct laser-sheet non-uniformities.

4.3.2. *Measurement of spanwise interfacial perturbations and image dewarping*

Spanwise interfacial measurements were performed as follows. First, the laser head and all associated optics were configured such that a vertical laser sheet was formed in a plane $x = 0.5$ cm downstream from the splitter plate. The laser sheet arrangement prevented placing the camera in a position directly normal to the laser sheet; otherwise the camera would then be physically located within the water channel. Thus, in order to image the laser sheet, the camera had to be located outside of the water channel. The camera was located approximately 40 cm from the midpoint of the trailing edge of the splitter plate, and the focal axis was located on the same horizontal plane as the splitter plate at an angle of $\approx 38^\circ$ with respect to the axis normal to the laser sheet. This angle was selected so that the camera could be located close enough to the laser sheet to satisfy resolution requirements, while keeping the angle small enough to keep the image calibrations feasible. The laser sheet was focused so that its thickness was < 1 mm near the centreplane of the mixing layer. A solution of Rhodamine 6G dye and water was injected into the channel using a syringe so that the imaging system could be focused. Once the camera was focused, the water channel pumps were activated, the mean advection velocities of each stream were adjusted to eliminate any shear, and then images of the fluorescing dye were captured. For reasons discussed earlier, the water channel was operated with no temperature difference between the two streams. Measurements were also performed at $A \approx 5.0 \times 10^{-4}$, with no difference found between the measurements performed at $A = 0$. Thus, the measured perturbations represent the interfacial perturbation imposed by the splitter plate and end-screen on the two-fluid interface in the spanwise direction. Once images of the two-fluid interface had been captured, the water channel was drained and a calibration card was placed at the same location as the laser sheet. The calibration card consisted of a grid of horizontal and vertical lines located at 1.27 cm intervals, and was used to eliminate any parallax and perspective errors introduced by positioning the camera at an oblique angle to the laser sheet. The calibration card was mounted between two sheets of clear 0.64 cm thick Plexiglas to ensure that the card remained flat during the course of an experiment. Once the calibration card was in place, an image of the grid was recorded with the same camera settings and location as used to capture the PLIF images. Images of the grid were used as a fiducial to calibrate the dewarping procedure described next.

Special consideration was given to the dewarping of the spanwise images. Other workers have used off-axis imaging and dewarping algorithms in stereoscopic PIV (Arroyo & Greated 1991; Willert 1997) and in other applications (Kent & Eaton 1982). However, the present experiments differ from previous implementations of off-axis imaging. The procedure used in the present investigation is the same robust, second-order dewarping method discussed by Pratt (1991) and van Oord (1997). The functional relationship between the warped coordinates (X_w, Y_w) and the dewarped coordinates (X_d, Y_d) is given by a second-order polynomial

$$\left.\begin{aligned} X_d(X_w, Y_w) &= a_0 + a_1 X_w + a_2 Y_w + a_3 X_w Y_w + a_4 X_w^2 + a_5 Y_w^2, \\ Y_d(X_w, Y_w) &= b_0 + b_1 X_w + b_2 Y_w + b_4 X_w Y_w + b_4 X_w^2 + b_5 Y_w^2, \end{aligned}\right\} \tag{21}$$

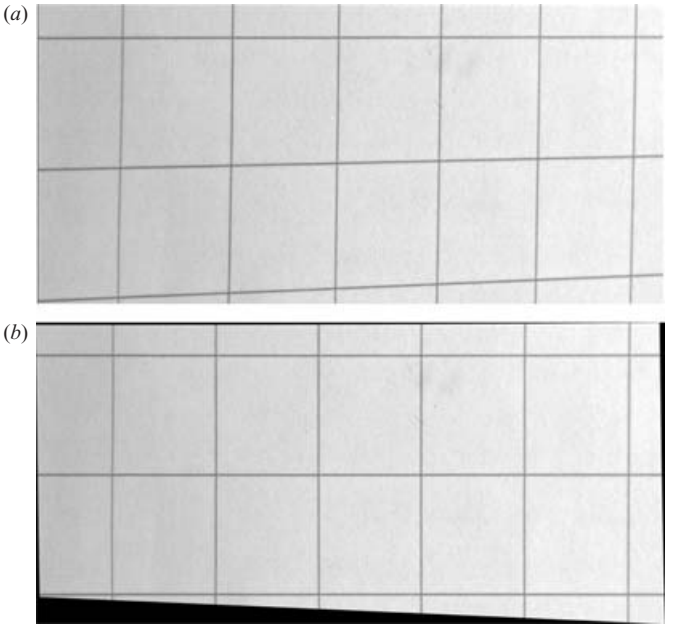

FIGURE 23. Raw image of (*a*) the warped calibration grid and (*b*) the dewarped calibration grid.

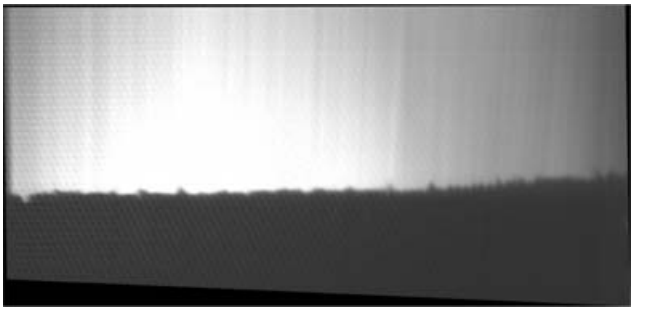

FIGURE 24. PLIF image of the spanwise interfacial perturbation at $x = 0.5\,\mathrm{cm}$ ($\tau \approx 0.02$) downstream from the splitter plate.

where a_i and b_i ($i = 0$–5) are calibrated coefficients. The unknown coefficients were determined from a least-squares fit relating 15 control points from the warped image of the calibration grid to their true physical location. Figure 23 shows the raw warped image of the calibration grid and a corrected image. A corrected PLIF image of the spanwise interfacial perturbation is shown in figure 24. Aside from dewarping the spanwise images, another correction was performed to account for the difference between the indices of refraction of air and water. This difference was readily determined from Snell's law of refraction, given the geometry of the experimental configuration, giving the correct width of the digital image.

4.3.3. *The interfacial perturbation spectrum*

Once a PLIF image had been corrected for perspective errors, the two-fluid interface was extracted by analysing the intensity values at each pixel location of the image.

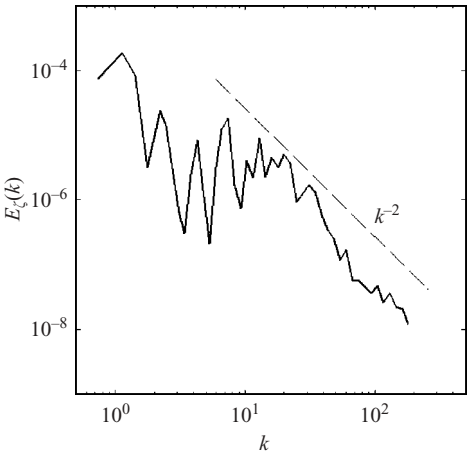

FIGURE 25. The spectrum of the spanwise interfacial perturbations at $x = 0.5$ cm ($\tau \approx 0.02$) downstream from the splitter plate.

A Canny-type edge filter was used to determine the interface between the fluorescing and non-fluorescing fluids. The Canny (1986) method identifies edges in the image at local maxima of the gradient of the intensity field, given a threshold value to eliminate spurious boundaries. Having measured the interfacial perturbation in the spanwise direction $\zeta(y)$, a corresponding perturbation variance spectrum $E_\zeta(k, \tau)$ was computed. Figure 25 shows this spectrum for one captured image at $x = 0.5$ cm ($\tau \approx 0.02$) downstream from the splitter plate, with the other images yielding similar spectra. The spectrum is broadbanded, with most of the energy content in the intermediate wavelengths $0.16 < \lambda < 8.0$ cm, well within the water channel width of 20 cm. The maximum 8 cm wavelength is attributed to the maximum width of the laser sheet achievable at the two-fluid interface. A k^{-2} scaling is evident in the wavenumber range of approximately $10 < k < 300$. This measured interfacial spectrum is similar to the spectrum of the surface roughness of glass ICF capsules which have measured interfacial perturbations that scale as k^{-2} in the lowest decade of modes (Milovich *et al.* 2004; Dimonte 2004).

Another finding from the spanwise PLIF measurements was that the waveform observed in repeated PLIF images appears unchanged. The lack of spanwise oscillations of the hot- and cold-water interface suggests that perturbations created by the splitter plate and end-screen do not include a velocity component in the spanwise direction, suggesting $\langle v'^2 \rangle \approx 0$ at the onset of the instability. Whereas the repeated PLIF images are capable of detecting spanwise velocity fluctuations, a mean spanwise velocity $\langle v \rangle$ cannot be detected, as the laser sheet is stationary and the fluid streams are not. To determine whether a mean velocity in the y-direction exists, a photograph of Nigrosene dye streaks shedding from the splitter plate was taken (figure 26). If a mean velocity field existed in the y-direction (spanwise), then streaklines of the dye would flow in both the x- and y-directions and not just along the x-axis. Inspection of figure 26 shows that the dye streaks just following the screen mesh (left-hand side of figure 26) advect only in the x-direction (streamwise) and do not travel cross-stream. Furthermore, inspection of the dye as it advects downstream in figure 26 reveals no apparent streamwise vortical motion. These observations, coupled with the PLIF images, support the claim that $\langle v \rangle \approx 0$ and $\langle v'^2 \rangle \approx 0$ in the initial conditions of this experiment.

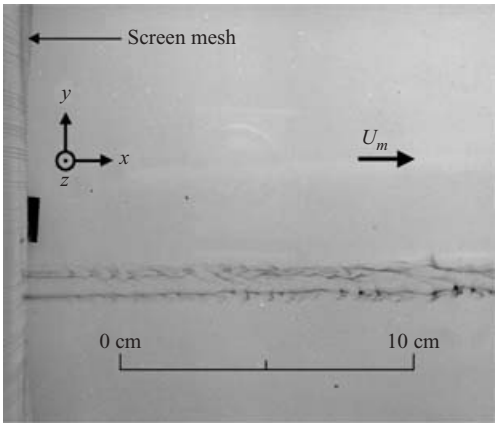

FIGURE 26. Top view of water channel showing advection of Nigrosene dye streaks.

The present measurements describe an initially anisotropic state in which the interfacial perturbations in the streamwise (x) and spanwise (y) directions are independent of one another and the only velocity perturbations large enough to be measured exist in the vertical and streamwise directions. Anisotropy of the initial conditions is expected when the initial perturbations are imposed by the experimental design. Examples of experimentally imposed initial conditions include: oscillation of separating boundary layers from the termination of the splitter plate in this experiment and in plate-withdrawal experiments (Linden & Redondo 1991; Linden *et al.* 1994; Dalziel *et al.* 1999); oscillation of accelerating tank experiments to produce a nominally two-dimensional perturbation (Emmons *et al.* 1960; Cole & Tankin 1973; Ratafia 1973; Popil & Curzon 1979); and planar or spherical laser-driven experiments that include surface perturbations at material interfaces (Kilkenny *et al.* 1994; Lindl 1998; Oron *et al.* 1999; Subramanian, Zebib & McQuillan 2005). It is difficult to quantify the initial perturbations in experiments that impose perturbations in two dimensions; however, several such experiments have yielded measurements for the single-mode instability evolution (Jacobs & Catton 1988; Wilkinson 2004). Additional modelling issues involving the specification of initial conditions are briefly discussed below.

5. Implications of the experimental results for the initialization of turbulent transport models and numerical simulations

An outstanding issue in turbulent transport modelling using the Reynolds-averaged Navier–Stokes (RANS) equations and other modelling approaches is the specification of the initial conditions satisfied by the turbulent fields. Moreover, the predictions of RANS models are inherently sensitive to the initial conditions chosen. The current initialization of RANS models is typically *ad hoc* and is often an iterative procedure involving the adjustment of model parameters and initial conditions until satisfactory predictions of mean flow quantities and low-order statistics are obtained. The initialization of RANS models to describe turbulent mixing induced by hydrodynamic instabilities, such as the Rayleigh–Taylor instability, presents several particular issues. Often turbulent transport models applied to Rayleigh–Taylor mixing are initialized using a phenomenological buoyancy-drag model to evolve the velocity fluctuations

until the width of the mixing layer becomes approximately equal to $2\Delta x$, where Δx is the grid spacing, at which time the fluctuations are used to provide an initial value of the turbulent kinetic energy, as in the K–l model of Youngs (1989, 1994). Similar issues are also shared by large-eddy simulation (LES) of hydrodynamic instability-driven turbulent mixing in which large-scale structures are generated from smaller-scale structures. In particular, the scale of the initial perturbations may be smaller than the grid size in either a transport model or in an LES, which raises the issue of how energy production at these unresolved small scales feeds into the turbulent transport quantities being evolved or into the explicit subgrid-scale model in an LES. However, LES of Rayleigh–Taylor instability-driven mixing is possible given a spatial resolution capable of resolving the initial perturbations (Cook *et al.* 2004).

In addition to complications associated with resolving the initial perturbations in a RANS model or in an LES, additional issues arise from the physical nature of the perturbations. In the present work, the spectra of velocity and density perturbations are highly anisotropic. There are several turbulent transport and subgrid-scale modelling implications associated with identifying and investigating the anisotropic state of the initial conditions. In numerical studies investigating the effects of multi-mode initial conditions on the evolution of Rayleigh–Taylor instability-driven mixing layers, an isotropic spectrum of initial interfacial perturbations is typically assumed (Youngs 1991; 1994; Cook & Dimotakis 2001; Cook *et al.* 2004; Dimonte *et al.* 2004; Ramaprabhu & Andrews 2004*b*; Ristorcelli & Clark 2004). Although the specific objectives of each study vary, the use of isotropic initial conditions represents idealized initial conditions for Rayleigh–Taylor instabilities, rather than an examination of a physical experiment or an application in which the Rayleigh–Taylor instability develops. For example, the evaluation of ICF target shell designs for the National Ignition Facility (NIF) at the Lawrence Livermore National Laboratory requires accurate modelling or simulation of the hydrodynamics and mixing (Haan *et al.* 1995, 2004; Amendt *et al.* 2002; Milovich *et al.* 2004). The perturbations present on the material interfaces in ICF capsules do not generally have an isotropic spectrum (Subramanian *et al.* 2005). Thus, turbulent transport and mixing models that do not include the detailed anisotropic structure of a mixing layer at early times (Youngs 1989; Steinkamp, Clark & Harlow 1999; Llor 2003) may not accurately model the unresolved hydrodynamics and mixing in imploding ICF capsules.

The measurements presented in this work characterized the initial conditions of the flow field as completely as possible and the early-time ($\tau < 1$) transient dynamics of the mixing layer as it approaches a self-similar state. While the exact quantitative results presented pertain to the parameters and initial conditions in the present experiment, the trends observed in both the mean and higher-order statistics are generally representative of Rayleigh–Taylor instabilities. For instance, Ristorcelli & Clark (2004) presented a set of direct numerical simulations of small-Atwood-number multimode miscible Rayleigh–Taylor mixing layers. While the simulations contained initial interfacial perturbations alone, many of the trends reported by Ristorcelli & Clark (2004) were similar to those reported here. In particular, the evolution of $\langle f_1'^2 \rangle$ or B_0, K_{f_1} and θ in both the simulations and experiment exhibit similar trends, albeit, with different magnitudes. One difference between the DNS and the experiment is the early-time evolution ($\tau < 1$) of centreplane velocity fluctuations, which are directly attributed to the differences in the initial conditions. The implications of these differences are clearly shown by Ramaprabhu & Andrews (2004*b*), where the trajectory taken by $\alpha = \langle w'^2 \rangle^{1/2}/(2Agt)$ is highly dependent upon the existence of initial velocity perturbations as self-similarity is approached.

6. Summary and conclusions

The initial multi-mode interfacial and velocity conditions have been experimentally measured in both the streamwise and spanwise directions in a statistically stationary miscible Rayleigh–Taylor instability-driven mixing layer. This investigation both extends and refines previous work on the measurement of the initial conditions in Rayleigh–Taylor instability-driven mixing layers. The inclusion of spanwise measurements in the current characterization of the initial conditions is novel with respect to the study of such flows, both in the measurement techniques used and in the results obtained. Combined with the streamwise density and velocity measurements, *the measurements presented here represent the most complete characterization of two-dimensional multi-mode initial interfacial perturbations with velocity conditions in a Rayleigh–Taylor mixing layer to date*. Comparisons of the initial density variance and vertical velocity variance spectra indicate that the initial evolution of density scales are driven by velocity fluctuations. The measurements also showed that the initial interfacial and velocity perturbations are anisotropic. This observation is important in that many models of Rayleigh–Taylor mixing-layer growth do not consider either the anisotropic initial conditions or the transition from an anisotropic state to a less anisotropic state in the late-time turbulent stage of the flow. Numerical simulations of a physical Rayleigh–Taylor mixing experiment must incorporate anisotropy into the initial conditions: the spectra of the initial fluctuations sufficient for the initialization of three-dimensional simulations of the water-channel experiment are presented in figures 7, 16 and 25.

In addition to a detailed characterization of the initial conditions of a Rayleigh–Taylor unstable fluid configuration, the time-evolution of the volume fraction probability distribution function, volume fraction variance and kurtosis, molecular mixing fraction, and density variance spectra were measured over $0 < \tau \leqslant 1.36$. These measurements indicate that an early-time transition exists in the level of molecular mixing in which, before the onset of strong nonlinearities and secondary Kelvin–Helmholtz instabilities, the interfacial area between the two fluids remains relatively small when compared to the area at later times. However, after the early-time onset of strong nonlinearities, the degree of molecular mixing within the flow steadily increases. It was shown that this increase in θ is associated with the decrease in $\langle f_1'^2 \rangle$ and with the shift in the energy-containing modes to smaller wavenumbers. The experimental data obtained in the present work have elucidated the complex initial conditions typically present in an experiment. In addition, this work has investigated the linear and nonlinear growth of the Rayleigh–Taylor instability (depending on the initial perturbation amplitudes and wavelengths), mode-coupling and growth of successively larger scales, and the transition to a well-mixed state. It is anticipated that these data, when coupled with high-resolution data from direct numerical simulations, can be used to develop criteria for the specification of initial conditions for both RANS models and for LES.

The authors thank Praveen Ramaprabhu, Wayne Kraft and Arindam Banerjee for their insightful comments on this research. This research was sponsored by the US Department of Energy National Nuclear Security Administration under the Stewardship Science Academic Alliances program through Department of Energy Research Grant #DE-FG03-02NA00060. This work was also performed under the auspices of the US Department of Energy by the University of California, Lawrence Livermore National Laboratory under Contract W-7405-Eng-48.

REFERENCES

Adrian, R. J. 1991 Particle-imaging techniques for experimental fluid mechanics. *Annu. Rev. Fluid Mech.* **23**, 261–304.

Adrian, R. J. 1997 Dynamic ranges of velocity and spatial resolution of particle image velocimetry. *Meas. Sci. Technol.* **8**, 1393–1398.

Adrian, R. J. 2005 Twenty years of particle image velocimetry. *Exps. Fluids* **39**, 159–169.

Allred, J. C., Blount, G. H. & Miller III, J. H. 1954 Experimental studies of Taylor instability. *Los Alamos Scientific Laboratory Rep.* LA-1600.

Amendt, P., Colvin, J. D., Tipton, R. E., Hinkel, D. E., Edwards, M. J., Landen, O. L., Ramshaw, J. D., Suter, L. J., Varnum, W. S. & Watt, R. G. 2002 Indirect-drive noncryogenic double-shell ignition targets for the National Ignition Facility: design and analysis. *Phys. Plasmas* **9**, 2221–2233.

Andrews, M. J. 1986 Turbulent mixing by Rayleigh–Taylor instability. PhD thesis. Imperial College of Science and Technology, London.

Andrews, M. J. & Spalding, D. B. 1990 A simple experiment to investigate two-dimensional mixing by Rayleigh–Taylor instability. *Phys. Fluids* A **2**, 922–927.

Anuchina, N. N., Kucherenko, Y. A., Neuvazhaev, V. E., Ogibina, V. N., Shibarshov, L. I. & Yakovlev, V. G. 1978 Turbulent mixing at an accelerating interface between liquids of different densities. *Izv. Akad Nauk. SSSR, Mekh. Zhidk. Gaza* **6**, 157–160.

Arroyo, M. P. & Greated, C. A. 1991 Stereoscopic particle image velocimetry. *Meas. Sci. Technol.* **2**, 1181–1186.

Bell, J. H. & Mehta, R. D. 1993 Effects of imposed spanwise perturbations on plane mixing-layer structure. *J. Fluid Mech.* **257**, 33–63.

Benedict, L. H. & Gould, R. D. 1996 Towards better uncertainty estimates for turbulence statistics. *Exps. Fluids* **22**, 129–136.

Bradshaw, P. 1966 The effect of initial conditions on the development of a free shear layer. *J. Fluid Mech.* **26**, 225–236.

Brouillette, M. 2002 The Richtmyer–Meshkov instability. *Annu. Rev. Fluid Mech.* **34**, 445–468.

Browand, F. K. & Weidman, P. D. 1976 Large scales in the developing mixing layer. *J. Fluid Mech.* **76**, 127–144.

Brown, G. L. & Roshko, A. 1974 On density effects and large structure in turbulent mixing layers. *J. Fluid Mech.* **64**, 775–816.

Canny, J. 1986 A computational approach to edge detection. *IEEE Trans. on Pattern Analysis and Machine Intelligence* **8**, 679–698.

Chandrasekhar, S. 1961 *Hydrodynamic and Hydromagnetic Stability*. Dover.

Cole, R. L. & Tankin, R. S. 1973 Experimental study of Taylor instability. *Phys. Fluids* **16**, 1810–1820.

Cook, A. W., Cabot, W. & Miller, P. L. 2004 The mixing transition in Rayleigh–Taylor instability. *J. Fluid Mech.* **511**, 333–362.

Cook, A. W. & Dimotakis, P. E. 2001 Transition stages of Rayleigh–Taylor instability between miscible fluids. *J. Fluid Mech.* **443**, 69–99; Corrigendum. *J. Fluid Mech.* **457**, 410–411 (2002).

Criminale, W., Jackson, T. L. & Joslin, R. D. 2003 *Theory and Computation in Hydrodynamic Stability*, Cambridge University Press.

Dai, Z., Tseng, L. K. & Faeth, G. M. 1994 Structure of round, fully developed, buoyant turbulent plumes. *J. Heat Transfer* **116**, 409–417.

Dalziel, S. B., Linden, P. F. & Youngs, D. L. 1999 Self-similarity and internal structure of turbulence induced by Rayleigh–Taylor instability. *J. Fluid Mech.* **399**, 1–48.

Dankwerts, P. V. 1952 The definition and measurement of some characteristics of mixtures. *Appl. Sci. Res.* **3**, 279–296.

Darbyshire, A. G. & Mullin, T. 1995 Transition to turbulence in constant-mass-flux pipe flow. *J. Fluid Mech.* **289**, 83–114.

Dimonte, G. 1999 Nonlinear evolution of the Rayleigh–Taylor and Richtmyer–Meshkov instabilities. *Phys. Plasmas* **6**, 2009–2015.

Dimonte, G. 2004 Dependence of turbulent Rayleigh–Taylor instability on initial perturbations. *Phys. Rev.* E **69**, 1–14.

Dimonte, G. & Schneider, M. 1996 Turbulent Rayleigh–Taylor instability experiments with variable acceleration. *Phys. Rev.* E **54**, 3740–3743.

Dimonte, G., Youngs, D. L., Dimits, A., Weber, S., Marinak, M., Wunsch, S., Garasi, C., Robinson, A., Andrews, M. J., Ramaprabhu, P., Calder, A. C., Fryxell, B., Biello, J., Dursi, L., MacNeice, P., Olson, K., Ricker, P., Rosner, R., Timmes, H., Tufo, F., Young, Y.-N. & Zingale, M. 2004 A comparative study of the turbulent Rayleigh–Taylor (RT) instability using high-resolution 3D numerical simulations: the Alpha-Group collaboration. *Phys. Fluids* **16**, 1668–1693.

Dimonte, G., Ramaprabhu, P., Youngs, D. L., Andrews, M. J. & Rosner, R. 2005 Recent advances in the turbulent Rayleigh–Taylor instability. *Phys. Plasmas* **12**, 1–6.

Drazin, P. G. 2002 *Introduction to Hydrodynamic Stability*. Cambridge University Press.

Drazin, P. G. & Reid, W. H. 2004 *Hydrodynamic Stability*, 2nd edn. Cambridge University Press.

Emmons, H. W., Chang, C. T. & Watson, B. C. 1960 Taylor instability of finite surface waves. *J. Fluid Mech.* **7**, 177–193.

Faisst, H. & Eckhardt, B. 2004 Sensitive dependence on initial conditions in transition to turbulence in pipe flow. *J. Fluid Mech.* **504**, 343–352.

Fallon, T. & Rogers, C. B. 2002 Turbulence-induced preferential concentration of solid particles in microgravity conditions. *Exps. Fluids* **33**, 233–241.

Fisher, C. E. & Ball, K. S. 1999 Plume dynamics in natural convection in a horizontal cylindrical annulus. *J. Heat Transfer* **121**, 598–602.

Grue, J., Jensen, A., Rusas, P. & Sveen, J. K. 2000 Breaking and broadening of internal waves. *J. Fluid Mech.* **413**, 181–217.

Haan, S. W. 1989 Onset of nonlinear saturation for Rayleigh–Taylor growth in the presence of a full spectrum of modes. *Phys. Rev.* A **39**, 5812–5825.

Haan, S. W., Pollaine, S. M., Lindl, J. D., Suter, L. J., Berger, R. L., Powers, L. V., Alley, W. E., Amendt, P. A., Futterman, J. A., Levedahl, W. K., Rosen, M. D., Rowley, D. P., Sacks, R. A., Shestakov, A. I., Strobel, G. L., Tabak, M., Weber, S. V., Zimmerman, G. B., Krauser, W. J., Wilson, D. C., Coggeshall, S. V., Harris, D. B., Hoffman, N. M. & Wilde, B. H. 1995 Design and modelling of ignition targets for the National Ignition Facility. *Phys. Plasmas* **2**, 2480–2487.

Haan, S. W., Amendt, P. A., Dittrich, T. R., Hammel, B. A., Hatchett, S. P., Herrmann, M. C., Hurricane, O. A., Jones, O. S., Lindl, J. D., Marinak, M. M., Munro, D., Pollaine, S. M., Salmonson, J. D., Strobel, G. L. & Suter, L. J. 2004 Design and simulation of indirect drive ignition targets for NIF. *Nucl. Fusion* **44**, S171–S176.

von Helmholtz, H. 1868 Über discontinuirliche Flüssigkeitsbewegungen. *Monats Königl. Preuss. Akad. Wiss.* **23**, 215–228.

Husain, Z. D. & Hussain, A. K. M. F. 1979 Axisymmetric mixing layer: Influence of the initial and boundary conditions. *AIAA J.* **17**, 48–55.

Jacobs, J. W. 1992 Shock-induced mixing of a light-gas cylinder. *J. Fluid Mech.* **234**, 629–649.

Jacobs, J. W. & Catton, I. 1988 Three-dimensional Rayleigh–Taylor instability. Part 2. Experiment. *J. Fluid Mech.* **187**, 353–371.

Kelvin, W. 1871 Hydrokinetic solutions and observations. *Phil. Mag.* **42**, 362–377.

Kent, J. C. & Eaton, A. R. 1982 Stereo photography of neutral density He-filled bubbles for 3-D fluid motion studies in an engine cylinder. *Appl. Optics* **21**, 904–912.

Kilkenny, J. D., Glendinning, S. G., Hann, S. W., Hammel, B. A., Lindl, J. D., Munro, D., Remington, B. A., Weber, S. V., Knauer, J. P. & Verdon, C. P. 1994 A review of the ablative stabilization of the Rayleigh–Taylor instability in regimes relevant to inertial confinement fusion. *Phys. Plasmas* **1**, 1379–1389.

Koop, G. K. 1976 Instability and turbulence in a stratified shear layer. PhD thesis, University of Southern California.

Kraft, W. N. 2004 Experimental investigation of a stratified buoyant wake. MS thesis. Texas A&M University.

Kucherenko, Yu. A., Neuvazhaev, V. E. & Pylaev, A. P. 1994 Behaviour of a region of gravity-induced turbulent mixing under conditions leading to separation. *Dokl. Akad. Nauk* **39**, 114–117.

Kucherenko, Yu. A., Balabin, S. I., Cherret, R. & Haas, J.-F. 1997 Experimental investigation into inertial properties of Rayleigh–Taylor turbulence. *Las. Part. Beams* **15**, 25–31.

Kucherenko, Yu. A., Balabin, S. I., Ardashova, R. I., Kozelkov, O. E., Dulov, A. V. & Romanov, I. A. 2003*a* Experimental study of the influence of the stabilizing properties of transitional layers on the turbulent mixing evolution. *Laser Part. Beams* **21**, 369–373.

Kucherenko, Yu. A., Pylaev, A. P., Murzakov, V. D., Belomestnih, A. V., Popov, V. N. & Tyaktev, A. A. 2003*b* Experimental study into the Rayleigh–Taylor turbulent mixing zone heterogeneous structure. *Laser Part. Beams* **21**, 375–379.

Kukulka, D. J. 1981 Thermodynamic and transport properties of pure and saline water. MS thesis, State University of New York at Buffalo.

Lee, M. P., McMillin, B. K., Palmer, J. L. & Hanson, R. K. 1992 Planar Fluorescence imaging of a transverse jet in a supersonic cross-flow. *J. Prop. Power* **8**, 729–735.

Linden, P. F. & Redondo, J. M. 1991 Molecular mixing in Rayleigh–Taylor instability. Part I: Global mixing. *Phys. Fluids* A **3**, 1269–1277.

Linden, P. F., Redondo, J. M. & Youngs, D. L. 1994 Molecular mixing in Rayleigh–Taylor instability. *J. Fluid Mech.* **265**, 97–124.

Lindl, J. D. 1998 *Inertial Confinement Fusion: The Quest for Ignition and Energy Gain using Indirect Drive*. Springer.

Llor, A. 2003 Bulk turbulent transport and structure in Rayleigh–Taylor, Richtmyer–Meshkov, and variable acceleration instabilities. *Laser Part. Beams* **21**, 305–310.

Marmottant, P. & Villermaux, E. 2004 On spray formation. *J. Fluid Mech.* **498**, 73–111.

Meshkov, E. E. 1969 Instability of the interface of two gases accelerated by a shock wave. *Sov. Fluid Dyn.* **4**, 101–104.

Meyer, T. R., Dutton, J. C. & Lucht, R. P. 2001 Experimental study of the mixing transition in a gaseous axisymmetric jet. *Phys. Fluids* **13**, 3411–3424.

Mi, J., Nobes, D. S. & Nathan, G. J. 2001 Influence of jet exit conditions on the passive scalar field of an axisymmetric jet. *J. Fluid Mech.* **432**, 91–125.

Mills, A. F. 1999 *Heat Transfer*, 2nd edn. Prentice–Hall.

Milovich, J. L., Amendt, P., Marinak, M. & Robey, H. 2004 Multimode short-wavelength perturbation growth studies for the National Ignition Facility double-shell ignition target designs. *Phys. Plasmas* **11**, 1552–1568.

Mueschke, N. J. 2004 An investigation of the influence of initial conditions on Rayleigh–Taylor mixing. MS thesis, Texas A&M University.

Mueschke, N. J. & Andrews, M. J. 2006 Investigation of scalar measurement error in diffusion and mixing processes. *Exps. Fluids* **40**, 165–175; Erratum. *Exps. Fluids* **40**, 176 (2006).

van Oord, J. 1997 The design of a stereoscopic DPIV-system. *Delft University of Technology Rep.* MEAH-161.

Oron, D., Sadot, O., Srebro, Y., Rikanati, A., Yedvab, Y., Alon, U., Erez, L., Erez, G., Ben-Dor, G., Levin, L. A., Ofer, D. & Shvarts, D. 1999 Studies in the nonlinear evolution of the Rayleigh–Taylor and Richtmyer–Meshkov instabilities and their role in inertial confinement fusion. *Laser Part. Beams* **17**, 465–475.

Papanicolaou, P. N. & List, E. J. 1987 Statistical and spectral properties of tracer concentration in round buoyant jets. *Intl J. Heat Mass Transfer* **30**, 2059–2071.

Pope, S. B. 2000 *Turbulent Flows*. Cambridge University Press.

Popil, R. & Curzon, F. L. 1979 Production of reproducible Rayleigh–Taylor instabilities. *Rev. Sci. Instrum.* **50**, 1291–1295.

Pratt, W. K. 1991 *Digital Image Processing*, 2nd edn. Wiley.

Press, W. H., Teukolsky, S. A., Vetterling, W. T. & Flannery, B. P. 2002 *Numerical Recipes in C: the Art of Scientific Computing*, 2nd edn. Cambridge University Press.

Ramaprabhu, P. 2003 On the dynamics of Rayleigh–Taylor mixing. PhD dissertation, Texas A&M University.

Ramaprabhu, P. & Andrews, M. 2003 Simultaneous measurements of velocity and density in buoyancy-driven mixing. *Exps. Fluids* **34**, 98–106.

Ramaprabhu, P. & Andrews, M. J. 2004*a* Experimental investigation of Rayleigh–Taylor mixing at small Atwood numbers. *J. Fluid Mech.* **502**, 233–271.

Ramaprabhu, P. & Andrews, M. J. 2004*b* On the initialization of Rayleigh–Taylor simulations. *Phys. Fluids* **16**, L59–L62.

Ramaprabhu, P., Dimonte, G. & Andrews, M. J. 2005 A numerical study of the influence of initial perturbations on the turbulent Rayleigh–Taylor instability. *J. Fluid Mech.* **536**, 285–319.

Ratafia, M. 1973 Experimental investigation of turbulent mixing by Rayleigh–Taylor instability. *Phys. Fluids* **16**, 1207–1210.

Rayleigh, Lord 1884 Investigation of the equilibrium of an incompressible heavy fluid of variable density. *Proc. Lond. Math. Soc.* **14**, 170–177.

Read, K. I. 1984 Experimental investigation of turbulent mixing by Rayleigh–Taylor instability. *Physica* D **12**, 45–58.

Reynolds, O. 1883 An experimental investigation of the circumstances which determine whether the motion of water in parallel channels shall be direct or sinuous and of the law of resistance in parallel channels. *Phil. Trans. R. Soc. Lond.* **186**, 123–164.

Richtmyer, R. D. 1960 Taylor instability in shock acceleration of compressible fluids. *Commun. Pure Appl. Maths.* **13**, 297–319.

Ristorcelli, J. R. & Clark, T. T. 2004 Rayleigh–Taylor turbulence: self-similar analysis and direct numerical simulations. *J. Fluid Mech.* **507**, 213–253.

Sharp, D. H. 1984 An overview of Rayleigh–Taylor instability. *Physica* D **12**, 3–18.

Snider, D. M. & Andrews, M. J. 1994 Rayleigh–Taylor and shear driven mixing with an unstable thermal stratification. *Phys. Fluids* A **6**, 3324–3334.

Steinkamp, M. J., Clark, T. T. & Harlow, F. H. 1999 Two-point description of two-fluid turbulent mixing – I. Model formulation. *Intl J. Multiphase Flow* **25**, 599–637.

Stillinger, D. C., Head, M. J., Helland, K. N. & Van Atta, C. W. 1983 A closed loop gravity-driven water channel for density stratified shear flow. *J. Fluid Mech.* **131**, 73–89.

Subramanian, P., Zebib, A. & McQuillan, B. 2005 Solutocapillary convection in spherical shells. *Phys. Fluids* **17**, 017103-1–017103-10.

Sveen, J. K. 2004 An introduction to MatPIV v. 1.6.1. eprint series, *Mech. Appl. Maths* **2**, 1–27.

Taylor, G. I. 1938 The spectrum of turbulence. *Proc. R. Soc. Lond.* A **164**, 476–490.

Taylor, G. I. 1950 The instability of liquid surfaces when accelerated in a direction perpendicular to their planes. *Proc. R. Soc. Lond.* **201**, 192–196.

Weygandt, J. H. & Mehta, R. D. 1995 Three-dimensional structure of straight and curved plane wakes. *J. Fluid Mech.* **282**, 279–311.

Wilkinson, J. P. 2004 Experimental study of the three-dimensional Rayleigh–Taylor instability for low Atwood numbers. MS thesis, University of Arizona.

Willert, C. 1997 Stereoscopic digital particle image velocimetry for application in wind tunnel flows. *Meas. Sci. Technol.* **8**, 1465–1479.

Williamson, C. H. K. 1996 Vortex dynamics in the cylinder wake. *Annu. Rev. Fluid Mech.* **28**, 477–539.

Wilson, P. N. 2002 A study of buoyancy and shear driven turbulence within a closed water channel. PhD dissertation, Texas A&M University.

Wilson, P. N. & Andrews, M. J. 2002 Spectral measurements of Rayleigh–Taylor mixing at low Atwood number. *Phys. Fluids* A **14**, 938–945.

Youngs, D. L. 1984 Numerical simulations of turbulent mixing by Rayleigh–Taylor instability. *Physica* D **12**, 32–44.

Youngs, D. L. 1989 Modelling turbulent mixing by Rayleigh–Taylor instability. *Physica D* **37**, 270–287.

Youngs, D. L. 1991 Three-dimensional numerical simulations of turbulent mixing by Rayleigh–Taylor instability. *Phys. Fluids* A **3**, 1312–1320.

Youngs, D. L. 1994 Three dimensional numerical simulation of turbulent mixing by Rayleigh–Taylor instabilities. *Laser Part. Beams* **12**, 725–750.